蘭州理工大學

科研成果汇总

学　　号: 161081102034

研 究 生: 徐晓冬

导　　师: 包广清 教授

研究方向: 智能电网控制技术

论文题目: 直流变压器中双有源桥 DC-DC变换器的优化控制研究

学　　科: 检测技术与自动化装置

学　　院: 电气工程与信息工程学院

入学时间: 2016年 09月

2024年 10月 31日

目　录

图书馆

文献检索报告

兰州理工大学图书馆 LUTLIB

报告编号：R2024-1054

机构：兰州理工大学 电气工程与信息工程学院

姓名：徐晓冬 [20120191]

著者要求对其在国内外学术出版物所发表的科技论著被以下数据库收录情况进行查证。

检索范围：

- 科学引文索引（Science Citation Index Expanded）：1900年-2024年
- 中国科学引文数据库（Chinese Science Citation Database）：1989年-2024年

检索结果：

检索类型	数据库	年份范围	总篇数	第一作者篇数
SCI-E 收录	SCI-EXPANDED	2021 - 2023	2	2
CSCD 收录	CSCD	2020	1	1

End

委托人声明：

本人委托兰州理工大学图书馆查询论著被指定检索工具收录情况，经核对检索结果，附件中所列文献均为本人论著，特此声明。

作　者（签字）：

完成人（签字）：陈超

完　成　日　期　：2024年10月30日

完成单位（盖章）：兰州理工大学图书馆信息咨询与学科服务部

（本检索报告仅限校内使用）

图书馆

文献检索报告
SCI-E 收录

兰州理工大学图书馆 LUTLIB

报告编号：R2024-1054 SCI-E 收录

数据库：科学引文索引 (Science Citation Index Expanded) 时间范围：2021年至2023年	作者姓名：徐晓冬 作者单位：兰州理工大学 电气工程与信息工程学院	检索人员：陈超 检索日期：2024年10月30日

检索结果：被 SCI-E 收录文献 2 篇

#	作者	地址	标题	来源出版物	文献类型	入藏号
1	**Xu, XD**; Bao, GQ; Wang, YW; Li, Q	[Xu, Xiaodong] Lanzhou Univ Technol, Coll Elect & Informat Engn, Lanzhou 730050, Peoples R China.; [Bao, Guangqing; Li, Qian] Southwest Petr Univ, Sch Elect Engn & Informat, Chengdu 610500, Peoples R China.; [Wang, Yuewu] Guangxi Univ Sci & Technol, Sch Automat, Liuzhou, Peoples R China.	Design of H8 Robust Controller With Load-Current Feedforward for Dual-Active-Bridge DC-DC Converters Considering Parameters Uncertainty	*IEEE ACCESS* 2023, 11: 72332-72342.	J Article	WOS:001035830200001
2	**Xu, XD**; Bao, GQ; Ma, M; Wang, YW	[Xu, Xiaodong; Bao, Guangqing] Lanzhou Univ Technol, Coll Elect & Informat Engn, Lanzhou, Peoples R China.; [Ma, Ming] State Grid Gansu Elect Power Corp, Wind Power Technol Ctr, Lanzhou, Peoples R China.; [Wang, Yuewu] Harbin Inst Technol, Sch Elect Engn & Automat, Harbin, Peoples R China.	Multi-Objective Optimization Phase-Shift Control Strategy for Dual-Active-Bridge Isolated Bidirectional DC-DC Converter	*INFORMACIJE MIDEM-JOURNAL OF MICROELECTRONICS ELECTRONIC COMPONENTS AND MATERIALS* 2021, 51 (3): 169-179.	J Article	WOS:000708853900003
					合计	2

图书馆

文献检索报告
CSCD 收录 (WOS)

SEARCH

兰州理工大学图书馆 LUTLIB

报告编号：R2024-1054 CSCD 收录 (WOS)

数据库：中国科学引文数据库 (Chinese Science Citation Database) 时间范围：2020年	作者姓名：徐晓冬 作者单位：兰州理工大学 电气工程与信息工程学院	检索人员：陈超 检索日期：2024年10月30日

检索结果：被 CSCD 收录文献 1 篇

#	作者	地址	标题	来源出版物	文献类型	入藏号
1	Xu Xiaodong; Bao Guangqing; Ma Ming; Wang Ningbo; Wang Yu; 徐晓冬; 包广清; 马明; 汪宁渤; 王裕	Xu Xiaodong, College of Electrical and Information Engineering, Lanzhou; University of Technology, Lanzhou, Gansu 730050, China.; Bao Guangqing, College of Electrical and Information Engineering,; Lanzhou University of Technology, Lanzhou, Gansu 730050, China.; Ma Ming, Electric Power Research Institute, State Grid Gansu Electric; Power Company;;Gansu Key Laboratory of Wind Power Integration Operation; and Control, ;;Gansu Key Laboratory of Wind Power Integration Operation; and Control, Lanzhou;;Lanzhou, ;; 730070;;730070.; Wang Ningbo, Electric Power Research Institute, State Grid Gansu; Electric Power Company;;Gansu Key Laboratory of Wind Power Integration; Operation and Control, ;;Gansu Key Laboratory of Wind Power Integration; Operation and Control, Lanzhou;;Lanzhou, ;; 730070;;730070.; Wang Yu, School of Automation,Guangdong University of Technology,; Guangzhou, Guangdong 510006, China.	Staircase Triangular Modulation Strategy for Modular Multilevel DC/DC Converter 应用于模块化多电平直流变换器的阶梯波调制策略	*Journal of Power Supply* 电源学报 2020, 18 (1): 116-121.	J Article	CSCD:6663251
					合计	1

IEEE Access
Multidisciplinary : Rapid Review : Open Access Journal

Received 15 June 2023, accepted 5 July 2023, date of publication 12 July 2023, date of current version 19 July 2023.

Digital Object Identifier 10.1109/ACCESS.2023.3294407

RESEARCH ARTICLE

Design of H∞ Robust Controller With Load-Current Feedforward for Dual-Active-Bridge DC–DC Converters Considering Parameters Uncertainty

XIAODONG XU[1], GUANGQING BAO[2], YUEWU WANG[3], AND QIAN LI[2]
[1]College of Electrical and Information Engineering, Lanzhou University of Technology, Lanzhou 730050, China
[2]School of Electrical Engineering and Information, Southwest Petroleum University, Chengdu 610500, China
[3]School of Automation, Guangxi University of Science and Technology, Liuzhou 545006, China

Corresponding author: Guangqing Bao (baogq03@163.com)

This work was supported in part by the National Natural Science Foundation of China under Grant 51967012, in part by the Central Government Funds for Guiding Local Scientific and Technological Development of China under Grant 2021ZYD0042, and in part by the Key Research and Development Program of Gansu Province under Grant 20YF8GA055.

ABSTRACT This paper proposes the design of H∞ robust controller with load-current feedforward for dual-active-bridge (DAB) dc-dc converters used in battery energy storage systems, aiming to ensure the dynamic response considering parameters uncertainty that the input voltage varies in a large range and the load is uncertain. Firstly, according to the state-space representation based on dual-phase-shift (DPS) control, a polytopic model of the DAB converter with two uncertain elements is established by convex optimization theory. Based on this model, linear matrix inequalities (LMIs) are then used to design the H∞ robust controller conveniently to minimize the influence of parameters uncertainty disturbance on the output voltage. At the same time, a regional closed-loop pole configuration technique is used to guarantee the dynamic response of the system under a wide range of operating conditions. Furthermore, an improved load-current feedforward control with lookup tables for phase-shift compensation is adopted to further enhance the dynamic response. Finally, an OPAL-RT hardware-in-loop platform with Texas Instruments TMS320F28377D microcontroller is used to verify the feasibility and effectiveness of the proposed H∞ robust controller.

INDEX TERMS Dual-active-bridge (DAB), dual-phase-shift (DPS), H∞controller, load-current feedforward, dynamic response.

I. INTRODUCTION

Benefitting from some advantages such as symmetrical structure, bidirectional power transmission, soft-switching performance, and easy module cascade [1], [2], [3], [4], dual-active-bridge (DAB) dc-dc converter has been widely adopted in industrial applications, such as dc microgrids [5], power electronic transformers [6], distributed generation systems [7], battery energy storage systems (BESS) [8], and medium voltage AC/ DC hybrid power grid [9]. In the above applications, high power density and high efficiency are typical demands for the DAB converter. Especially in BESS, the DAB converter is simultaneously required to guarantee robust dynamic response under parameters uncertainty that the input voltage varies in a large range and the load is uncertain.

In recent years, many control schemes integrated with various phase-shift control strategies have been investigated to ensure the dynamic response of the DAB converter. In an early literature [10], dynamic response comparisons of traditional single-phase-shift (SPS), dual-phase-shift (DPS), and model-based phase-shift control (MPSC) for the DAB

The associate editor coordinating the review of this manuscript and approving it for publication was Vitor Monteiro.

converter are evaluated, with a conclusion that MPSC shows the best dynamic response. In [11], based on SPS control, a load-current feedforward (LCFF) compensation solution is presented to enhance the transient response of the DAB converter against the load change; however, the input voltage fluctuation is not considered. By introducing virtual direct power control (VDPC) into SPS control [12], a VDPC method is proposed to obtain zero overshoot and robust dynamic response when suffering load or input voltage transient disturbances. By combing improved MPSC with LCFF control for the SPS-controlled DAB converter, as presented in [13], the improved strategy can guarantee a faster dynamic response to all the operating ranges. Besides, a discrete extended-phase-shift (EPS) control with low computational complexity is proposed to achieve rapid dynamic response when both load and input voltage change [14]. Moreover, in order to reduce the load current sensor used in the above schemes to lower the hardware cost of the DAB converter, an extended state observer (ESO)-based sensor-reduction control with DPS [15] and a load-current estimating method with switching-period delay compensation [16] are proposed to boost dynamic responses.

Another method for dynamic response improvement for the DAB converter is to engage advanced control schemes, such as model predictive control (MPC), artificial neural network (ANN), sliding mode control, H∞ robust control and linear-quadratic regulator control. Combined with simple SPS, a non-linear MPC with phase-shift compensation is presented to enhance dynamic response against the disturbance of input voltage and load [17]. For DAB converter fast feeding constant power loads or pulsed power loads applied in dc microgrids, an ANN-based MPC method [18], a deep reinforcement learning-based intelligent nonlinear controller [19], an ANN-based active disturbance rejection control with ESO [20], and a moving discretized control set MPC (MDCS-MPC) with SPS [21] are proposed; however, they are extremely complex with a heavy computational burden. In order to lower the computational burden, by utilizing only two prediction horizons, an MDCS-MPC with triple-phase-shift (TPS) is proposed in [22]. Besides, though sliding mode control can provide the DAB converter with a fast transient response for load variations and robust control for parameter uncertainties [23], [24], heavy computation is still an issue. Similar to some advanced control schemes, H∞ robust controller is suited for improving the system stability and performance for power inverters/converters [25], [26], [27], [28], especially when the parameters are uncertain. However, few papers can be found on the application of the DAB converter. To effectively address the system uncertainty and parameter perturbations of the DAB converter, an H∞ mixed sensitivity robust control is presented in [29], which finally obtains a third-order controller by solving Riccati equations, but the selection of the appropriate weighting function is a challenge. Furthermore, To cover such challenges, by using linear matrix inequalities (LMIs) to derive the optimized control parameters, an LMI

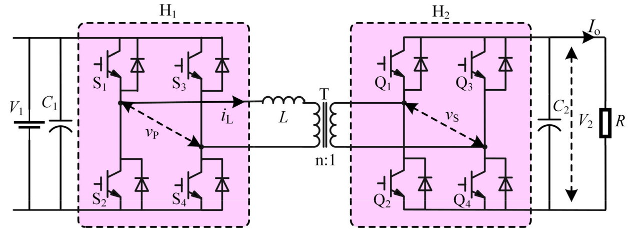

FIGURE 1. Topology configuration of DAB converter.

H∞ robust control is early used to design controllers for boost converters [30], but the disturbance of input voltage is not considered. And then, a robust LMIs-based linear-quadratic regulator control for the DAB converter is improved in [31], which can enhance dynamic performances when both input voltage and load change and achieve robust stability. However, the above two robust controllers in [29] and [31] for the DAB converter are combined with SPS, lacking control freedom compared to DPS, EPS, or TPS.

Thus, in this paper, for more control freedom, based on DPS control, an H∞ robust controller with LCFF for DAB dc-dc converters is proposed, aiming to ensure the dynamic response of the DAB converter considering parameters uncertainty that the input voltage varies in a large range and the load is uncertain. The main contribution of this paper is the establishment of a polytopic model for the DAB converter based on DPS control considering parameters uncertainty, so as to conveniently design the H∞ robust controller by using the LMIs to minimize the influence of parameters uncertainty disturbance on the output voltage. In addition, a regional closed-loop pole configuration technique based on LMIs is used to guarantee the acceptable dynamic response, while an LCFF with lookup tables for phase-shift compensation is improved to further enhance the dynamic response.

This paper is organized as follows. Firstly, a polytopic model of the DAB converter with two uncertain elements is established in Section II. Based on this model, LMIs are then used to design the H∞ robust controller in Section III, with a regional closed-loop pole configuration technique to cope with the system under a wide range of input voltage conditions. Then, an improved LCFF control scheme is adopted to further ensure the dynamic response. Finally, Section IV provides the experimental results obtained from an OPAL-RT hardware-in-loop platform to verify the proposed H∞ robust controller.

II. POLYTOPIC MODEL OF AN UNCERTAIN DAB CONVERTER UNDER DPS CONTROL

A. OPERATION PRINCIPLE AND SMALL-SIGNAL MODEL OF A DAB CONVERTER

Fig. 1 describes the topology of the DAB converter. Two full bridges H_1 and H_2 connect each other with an auxiliary inductor L and an isolated transformer (turn ratio n = 5:8 in this paper). C_1 and C_2 are the dc capacitors. $S_1 \sim S_4$ and

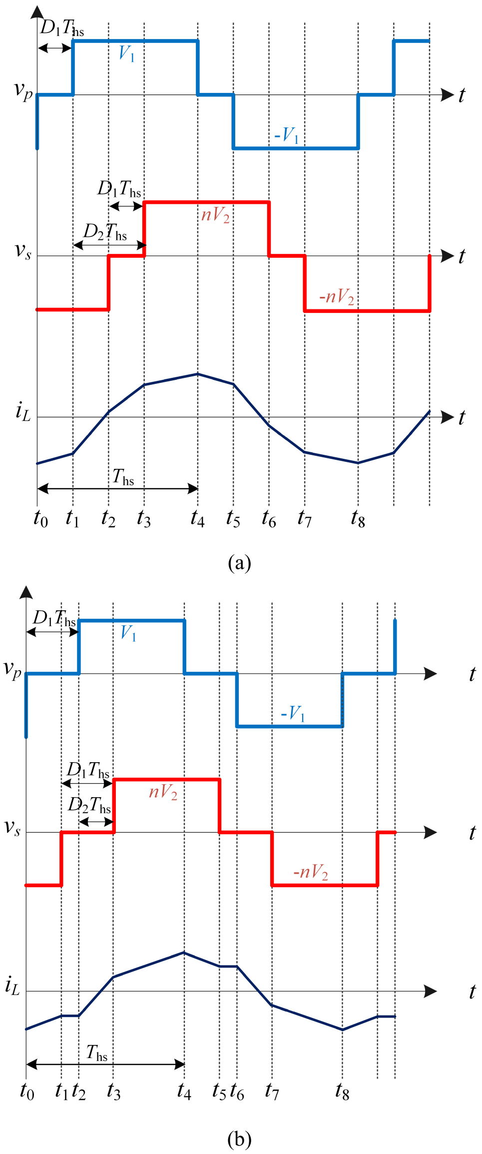

FIGURE 2. Voltage and current waveforms of DAB converter under DPS control: (a) $0 \leq D_1 \leq D_2 \leq 1$, (b) $0 \leq D_2 \leq D_1 \leq 1$.

$Q_1 \sim Q_4$ are two groups of switches in the two full bridges, respectively. V_1 is the dc input voltage, and V_2 is the dc output voltage. v_p and v_s represent the high frequency ac voltages generated by H_1 and H_2, respectively. i_L is the inductor current, and I_o is the load current.

Generally, the DPS-based DAB converter has two degrees of freedom with inner phase-shift ratio and outer phase-shift ratio, which mainly operates in two modes [32]: $0 \leq D_1 \leq D_2 \leq 1$ and $0 \leq D_2 \leq D_1 \leq 1$, as shown in Fig. 2. D_1 represents the inner phase-shift ratio, which is the phase shift between switches S_1 and S_4 or Q_1 and Q_4; D_2 represents the outer phase-shift ratio, which is the phase shift between switches S_1 and Q_1; and T_{1s} is half of the switching cycle. As shown in Fig. 2, under DPS control, the ac voltage output from two full bridges are three-level waves with an equal duty cycle and a specific phase shift. In the existing literature, D_1 is usually used to improve the performances of the DAB converter, such as reactive power [33], current stress [34], and efficiency performance [35]; and D_2 is obtained from a closed-loop control. In this paper, D_1 is directly set to 0.2 for simplicity, so as to focus on the design of proposed H∞ robust controller with D_2.

According to Fig. 1 and Fig. 2, in a switching cycle (T_s), the DAB converter has eight operation modes. Moreover, the inductor current and the ac voltage of the two full bridges show symmetrical waveforms, so the state-space averaging model can be described in half a switching cycle.

In the DAB converter, when the condition meets $0 \leq D_1 \leq D_2 \leq 1$, the inductor current at t_0, t_1, t_2, t_3, t_4 can be described [36]:

$$\begin{cases} i_L(t_0) = \dfrac{V_1}{4f_sL}(D_1-1) - \dfrac{nV_2}{4f_sL}(2D_2+D_1-1) \\ i_L(t_1) = \dfrac{V_1}{4f_sL}(D_1-1) + \dfrac{nV_2}{4f_sL}(1+D_1-2D_2) \\ i_L(t_2) = \dfrac{V_1}{4f_sL}(2D_2-D_1-1) + \dfrac{nV_2}{4f_sL}(1-D_1) \\ i_L(t_3) = \dfrac{V_1}{4f_sL}(2D_2+D_1-1) - \dfrac{nV_2}{4f_sL}(D_1-1) \\ i_L(t_4) = \dfrac{V_1}{4f_sL}(1-D_1) + \dfrac{nV_2}{4f_sL}(2D_2+D_1-1) \end{cases} \tag{1}$$

where $f_s = 1/T_s$ is the switching frequency.

As can be seen from Fig. 1 and Fig. 2, it can be obtained four differential equations across the output capacitor C_2 between each time interval of $t_0 \sim t_4$ according to Kirchhoff current law:

$$\begin{cases} C_2\dfrac{dv_2}{dt} = -\bar{i}_{L1} - \dfrac{v_2}{R} & t \in [0, D_1T_{hs}] \\ C_2\dfrac{dv_2}{dt} = -\bar{i}_{L2} - \dfrac{v_2}{R} & t \in [D_1T_{hs}, D_2T_{hs}] \\ C_2\dfrac{dv_2}{dt} = -\dfrac{v_2}{R} & t \in [D_2T_{hs}, (D_1+D_2)T_{hs}] \\ C_2\dfrac{dv_2}{dt} = -\bar{i}_{L4} - \dfrac{v_2}{R} & t \in [(D_1+D_2)T_{hs}, T_{hs}] \end{cases} \tag{2}$$

where $\bar{i}_{L1}$, $\bar{i}_{L2}$, and $\bar{i}_{L4}$ represent the inductor current averaging values, which are:

$$\begin{cases} \bar{i}_{L1} = \dfrac{i_L(t_0)+i_L(t_1)}{2} \\ \bar{i}_{L2} = \dfrac{i_L(t_1)+i_L(t_2)}{2} \\ \bar{i}_{L4} = \dfrac{i_L(t_3)+i_L(t_4)}{2} \end{cases} \tag{3}$$

Furthermore, extending the four differential equations in (2) to the entire switching cycle of the DAB converter, time-averaging scheme can be used to derive the final state-space averaging model:

$$C_2\frac{dv_2}{dt} = \frac{nV_1}{4f_sL}[2d_2(1-d_2) - D_1^2] - \frac{v_2}{R} \tag{4}$$

where d_2 is the outer phase-shift ratio containing ac disturbance.

In order to further derive the small-signal model of the DAB converter, low-frequency ac small-signal disturbance is introduced as

$$\begin{cases} v_2 = V_{2ss} + \hat{v}_2 \\ d_2 = D_{2ss} + \hat{d}_2 \end{cases} \tag{5}$$

where V_{2ss} and D_{2ss} are the dc component of the output voltage and outer phase-shift ratio, respectively, and $\hat{v}_2$ and $\hat{d}_2$ are the corresponding ac components, respectively. Substituting (4) into (5) and ignoring the small-signal ac component $\hat{d}_2^2$, the small-signal model of the DAB converter is derived as

$$\frac{d\hat{v}_2}{dt} = \frac{nV_1}{2f_sLC_2}(1 - 2D_{2ss})\hat{d}_2 - \frac{\hat{v}_2}{RC_2} \tag{6}$$

Aiming to guarantee accurate tracking control for the output voltage, another state variable $x_2(t) = \int \left[V_{ref} - v_2(t)\right] dt$ representing the integral of the corresponding voltage error is introduced. Thus, combining (5) and (6), the state-space representation of the DAB converter is written as

$$\begin{cases} \dot{\boldsymbol{x}}(t) = \boldsymbol{A}\boldsymbol{x}(t) + \boldsymbol{B}_w w(t) + \boldsymbol{B}_u u(t) + \boldsymbol{B}_{ref} V_{ref} \\ z(t) = \boldsymbol{C}_z \boldsymbol{x}(t) + \boldsymbol{D}_{zw} w(t) + \boldsymbol{D}_{zu} u(t) \end{cases} \tag{7}$$

where $\boldsymbol{x}(t) = \begin{bmatrix} v_2(t) \\ x_2(t) \end{bmatrix}$, $w(t) = [i_o(t)]$, $u(t) = [d_2(t)]$, $z(t) = [v_2(t)]$. The vector $\boldsymbol{w}$ represents the disturbance of the load-current i_o. The output z represents the output voltage v_2. Moreover, the state-space matrices are as follows

$$\begin{aligned} &\boldsymbol{A} = \begin{bmatrix} -\frac{1}{RC_2} & 0 \\ -1 & 0 \end{bmatrix}, \quad \boldsymbol{B}_w = \begin{bmatrix} -\frac{1}{C_2} \\ 0 \end{bmatrix}, \\ &\boldsymbol{B}_u = \begin{bmatrix} \frac{nV_1}{2f_sLC_2}(1 - 2D_{2ss}) \\ 0 \end{bmatrix}, \quad \boldsymbol{B}_{ref} = \begin{bmatrix} 0 \\ 1 \end{bmatrix}, \\ &\boldsymbol{C}_z = \begin{bmatrix} 1 & 0 \end{bmatrix}, \quad \boldsymbol{D}_{zw} = [0], \ \boldsymbol{D}_{zu} = [0] \end{aligned} \tag{8}$$

where $\boldsymbol{A}$ is the state matrix; $\boldsymbol{B}_w$ is the disturbance matrix; $\boldsymbol{B}_u$ is the control matrix; $\boldsymbol{B}_{ref}$ is the reference matrix; $\boldsymbol{C}_z, \boldsymbol{D}_{zw}$ and $\boldsymbol{D}_{zu}$ are output matrices.

Similarly, when the condition satisfies $0 \le D_2 \le D_1 \le 1$, the state-space averaging model is derived as

$$C_2 \frac{dv_2}{dt} = \frac{nV_1}{4f_sL} d_2(2 - 2D_1 - d_2) - \frac{v_2}{R} \tag{9}$$

And the corresponding small-signal model of the DAB converter is derived as

$$\frac{d\hat{v}_2}{dt} = \frac{nV_1}{2f_sLC_2}(1 - D_1 - D_{2ss})\hat{d}_2 - \frac{\hat{v}_2}{RC_2} \tag{10}$$

So as the state-space matrices are obtained as

$$\begin{aligned} &\boldsymbol{A} = \begin{bmatrix} -\frac{1}{RC_2} & 0 \\ -1 & 0 \end{bmatrix}, \quad \boldsymbol{B}_w = \begin{bmatrix} -\frac{1}{C_2} \\ 0 \end{bmatrix}, \\ &\boldsymbol{B}_u = \begin{bmatrix} \frac{nV_1}{2f_sLC_2}(1 - D_1 - D_{2ss}) \\ 0 \end{bmatrix}, \quad \boldsymbol{B}_{ref} = \begin{bmatrix} 0 \\ 1 \end{bmatrix}, \\ &\boldsymbol{C}_z = \begin{bmatrix} 1 \ 0 \end{bmatrix}, \quad \boldsymbol{D}_{zw} = [0], \ \boldsymbol{D}_{zu} = [0] \end{aligned} \tag{11}$$

B. POLYTOPIC MODEL CONSIDERING THE UNCERTAINTY OF INPUT VOLTAGE AND LOAD

In BESS, considering that the terminal voltage varies widely during battery charging and discharging and the power transmitted to the dc bus depends on the load, that is, the input voltage V_1 of the DAB converter is not a stable value, and the load is uncertain. Therefore, the polytopic model in convex optimization theory can be adopted to build the system model of the DAB converter so that LMI optimization methods can be easily applied to solve the closed-loop controller [30], [37]. This method ensures system stability at different operating points, as well as optimal immunity to disturbances and transient performance. In modelling, the input voltage and the load are taken as uncertainties, that is, a vector $\boldsymbol{p} = (1/R, V_1)$ is used to include the two uncertain terms, which is constrained in the polytopic model. Thus, for the DAB converter, based on the state-space representation (7), the polytopic model can be formed as.

$$\begin{cases} \dot{\boldsymbol{x}}(t) = \boldsymbol{A}(\boldsymbol{p})\boldsymbol{x}(t) + \boldsymbol{B}_w w(t) + \boldsymbol{B}_u(\boldsymbol{p})u(t) + \boldsymbol{B}_{ref} V_{ref} \\ z(t) = \boldsymbol{C}_z x(t) + \boldsymbol{D}_{zw} w(t) + \boldsymbol{D}_{zu} u(t) \end{cases} \tag{12}$$

where the state-space matrices $\boldsymbol{A}(\boldsymbol{p})$ and $\boldsymbol{B}_u(\boldsymbol{p})$ are determined by uncertain terms grouped in the vector $\boldsymbol{p}$. In this paper, $\boldsymbol{A}(\boldsymbol{p})$ and $\boldsymbol{B}_u(\boldsymbol{p})$ have a linear relationship with each uncertain parameter of vector $\boldsymbol{p}$, respectively.

Generally, the introduced vector $\boldsymbol{p}$ contains N uncertain parameters, that is $\boldsymbol{p} = (p_1, p_2, \ldots, p_N)$. Each uncertain p_i is a bounded parameter, which is constrained within a specific range as

$$p_i \in \left[\underline{p}_i, \bar{p}_i\right] \tag{13}$$

Moreover, the possible values of vector $\boldsymbol{p}$ are hold within a hyperrectangle in the parameter space R^N with $L = 2^N$ vertices $\{v_1, v_2, \ldots, v_N\}$. And the system matrix $[\boldsymbol{A}(\boldsymbol{p}), \boldsymbol{B}_u(\boldsymbol{p})]$ for each vertex v_i corresponds to the extrema of a convex polytope, noted $Co\{G_1, G_2, \ldots, G_L\}$. Therefore, the system matrix $[\boldsymbol{A}(\boldsymbol{p}), \boldsymbol{B}_u(\boldsymbol{p})]$ can be contained as

$$\begin{aligned} [\boldsymbol{A}(\boldsymbol{p}), \boldsymbol{B}_u(\boldsymbol{p})] &\in Co\{G_1, G_2, \ldots, G_L\} \\ &:= \left\{ \sum_{i=1}^{L} \lambda_i G_i, \lambda_i \ge 0, \sum_{i=1}^{L} \lambda_i = 1 \right\} \end{aligned} \tag{14}$$

A detailed description of the convex polytope can be found in [37] and [38].

When specific to this paper for the DAB converter, the input voltage V_1 and the load resistance R are considered uncertainties ($N = 2$), while the rest elements are assumed constant. Thus, the two parameters of vector $\boldsymbol{p} = (1/R, V_1)$ are constrained in the following boundaries:

$$1/R \in \left[1/R_{\max}, 1/R_{\min}\right], \quad V_1 \in [V_{1\min}, V_{1\max}] \tag{15}$$

Furthermore, the polytopic model of the DAB converter established in this paper has $L = 2^N = 4$ vertices that determine the uncertain matrices $\boldsymbol{A}(\boldsymbol{p})$ and $\boldsymbol{B}_u(\boldsymbol{p})$. When the

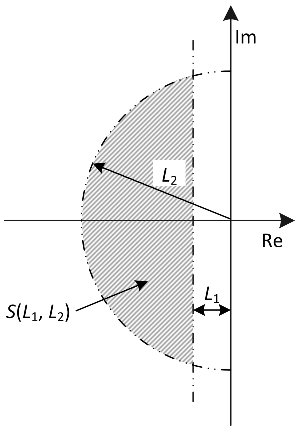

FIGURE 3. LMI region $S(L_1, L_2)$.

condition meets $0 \leq D_1 \leq D_2 \leq 1$, the vertices are obtained as:

$$\begin{aligned}
&\boldsymbol{A}_1 = \begin{bmatrix} -\frac{1}{R_{\max}C_2} & 0 \\ -1 & 0 \end{bmatrix}, \quad \boldsymbol{B}_{u1} = \begin{bmatrix} \frac{nV_{1\min}}{2f_sLC_2}(1-2D_{2ss}) \\ 0 \end{bmatrix}, \\
&\boldsymbol{A}_2 = \begin{bmatrix} -\frac{1}{R_{\min}C_2} & 0 \\ -1 & 0 \end{bmatrix}, \quad \boldsymbol{B}_{u2} = \begin{bmatrix} \frac{nV_{1\max}}{2f_sLC_2}(1-2D_{2ss}) \\ 0 \end{bmatrix}, \\
&\boldsymbol{A}_3 = \boldsymbol{A}_2, \quad \boldsymbol{B}_{u3} = \boldsymbol{B}_{u1}, \\
&\boldsymbol{A}_4 = \boldsymbol{A}_1, \quad \boldsymbol{B}_{u4} = \boldsymbol{B}_{u2}
\end{aligned} \tag{16}$$

III. PROPOSED H∞ ROBUST SOLUTION WITH LOAD-CURRENT FEEDFORWARD

In this section, firstly, H∞ control is adopted to effectively suppress the influence of system parameter perturbation on output and minimize the gain of disturbance on output. Secondly, in order to improve the dynamic settling time of the system, the poles of the closed-loop system are configured in a specific region. In addition, an improved LCFF control is adopted to enhance the dynamic response.

A. H∞ CONTROLLER BASED ON LMIS

For the polytopic model described in (12), there exists a state-feedback controller whose role is to achieve a minimum gain of the disturbance to the output. For the design of robust control systems, the gain of the disturbance to the output is usually transformed into the problem of H∞ norm bound. The H∞ norm can be explained by amplitude-frequency characteristics of a transfer function $f(s)$, which is effective for problems related to model uncertainty. Considering that the transfer function from the disturbance w to the output z is $H(s)$, the corresponding H∞ norm is expressed as

$$\|H(s)\|_\infty \sup_{w \neq 0} \frac{\|z\|_2}{\|w\|_2} \tag{17}$$

where $\|\cdot\|_\infty$ represents the infinity norm and $\|\cdot\|_2$ represents the Euclidian norm.

Considering that the smaller the H∞ norm, the better the suppression of the disturbance, when a minimum H∞ norm γ is guaranteed, there exists a state-feedback H∞ controller $(u(t) = d_2(t) = \boldsymbol{K}x(t))$ if and only if a positive definite matrix $\boldsymbol{W} \in \boldsymbol{R}^{n\times n}$ and a matrix $\boldsymbol{Y} \in \boldsymbol{R}^{n\times n}$ make the following LMI hold

$$\begin{bmatrix} \boldsymbol{AW} + \boldsymbol{WA}^{\mathrm{T}} + \boldsymbol{B}_u\boldsymbol{Y} + \boldsymbol{Y}^{\mathrm{T}}\boldsymbol{B}_u^{\mathrm{T}} & \boldsymbol{B}_w & \boldsymbol{WC}_z^{\mathrm{T}} + \boldsymbol{Y}^{\mathrm{T}}\boldsymbol{D}_{zu}^{\mathrm{T}} \\ \boldsymbol{B}_w^{\mathrm{T}} & -\gamma \boldsymbol{I} & 0 \\ \boldsymbol{C}_z\boldsymbol{W} + \boldsymbol{D}_{zu}\boldsymbol{Y} & 0 & -\gamma\boldsymbol{I} \end{bmatrix} < 0 \tag{18}$$

Thus, the H∞ controller is obtained by $\boldsymbol{K} = \boldsymbol{YW}^{-1}$. Proof of (18) can be found in [39]. For all the vertices $\{G_1, G_2, \ldots, G_L\}$ in the polytopic model of the DAB converter, it is sufficient to satisfy (18) to solve the stability problem for different steady-state operating points of the system.

B. POLE PLACEMENT LMIS

In the classical control theory, the amplitude-frequency and phase-frequency characteristics of the open-loop system are obtained through the transfer function so as to design the controller according to the Bode diagram. However, the classical control method usually assigns the closed-loop poles precisely, which is not suite for the system with the imprecision of the model and the existence of various disturbances.

Thus, in this paper, LMI is used to directly assign the closed-loop poles of the system in a given region of the complex plane to ensure some desired dynamic characteristics, such as decay rate, settling time, damping ratio, etc. As shown in Fig. 3, in the region $S(L_1, L_2)$ of the complex plane for the system [40], the assigned closed-loop poles $(x \pm \mathrm{j}y)$ should meet

$$x < -L_1 < 0, \quad |x \pm \mathrm{j}y| < L_2 \tag{19}$$

where L_1 and L_2 are two values given by the designer. L_1 is used to determine a minimum decay rate, and L_2 is used to limit a maximum natural frequency.

Considering the decay rate constrained by L_1, the following LMI is obtained

$$\boldsymbol{AW} + \boldsymbol{WA}^{\mathrm{T}} + \boldsymbol{B}_u\boldsymbol{Y} + \boldsymbol{Y}^{\mathrm{T}}\boldsymbol{B}_u^{\mathrm{T}} + 2L_1\boldsymbol{W} < 0 \tag{20}$$

Furthermore, the constraint of the natural frequency according to L_2 involves the following LMI

$$\begin{bmatrix} -L_2\boldsymbol{W} & \boldsymbol{WA}^{\mathrm{T}} + \boldsymbol{Y}^{\mathrm{T}}\boldsymbol{B}_u^{\mathrm{T}} \\ \boldsymbol{AW} + \boldsymbol{B}_u\boldsymbol{Y} & -L_2\boldsymbol{W} \end{bmatrix} < 0 \tag{21}$$

A detailed explanation of LMIs (20) and (21) can be found in [40], and it is proven in [40] that when the system with the H∞ robust controller $u(t) = d_2(t) = \boldsymbol{K}x(t) = \boldsymbol{YW}^{-1}x(t)$ meets LMIs (20) and (21), the closed-loop poles $(x \pm \mathrm{j}y)$ can be directly assigned in the given region $S(L_1, L_2)$.

Here, in this paper, all the vertices $\{G_1, G_2, \ldots, G_L\}$ in the polytopic model of the DAB converter need to satisfy LMIs not only (18) but also (20) and (21), so that the closed-loop poles of the system under different stable operating points are

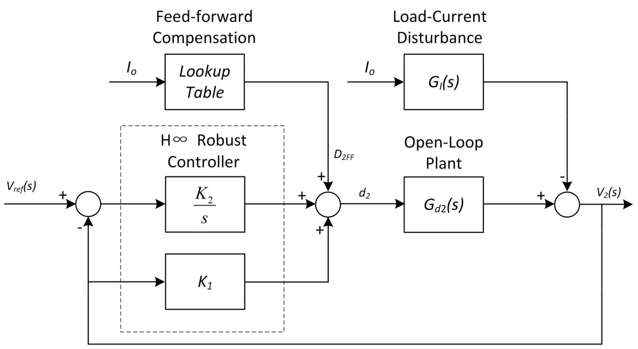

FIGURE 4. H∞ robust control with load-current feedforward compensation for DAB converter.

TABLE 1. Lookup tables for load-current feedforward compensation.

Input Voltage	250 V	300 V	350 V	400 V	450 V
$0\leqslant D_1\leqslant D_2\leqslant 1$	0.0202	0.0169	0.0144	0.0126	0.0112
$0\leqslant D_2\leqslant D_1\leqslant 1$	0.0171	0.0143	0.0122	0.0107	0.0095

assigned in the given region $S(L_1, L_2)$ to meet the acceptable dynamic performance of the system.

Thus, by combining LMIs (18), (20) and (21), the LMI synthesis method for the proposed H∞ robust controller with pole placement can be summarized as the following optimization problem:

$$\begin{cases} \min\limits_{Y,\,W} \quad \gamma \quad \text{subject to (18), (20) } and \text{ (21)} \\ \qquad\qquad \forall \{G_i\}, \quad i = 1, \ldots, L \end{cases} \tag{22}$$

The solving procedure of the optimization problem (22) consists of finding a set of common matrices $\boldsymbol{Y}$ and $\boldsymbol{W}$ by solving LMIs, so as to obtain the H∞ robust controller $u(t) = d_2(t) = \boldsymbol{K}x(t) = \boldsymbol{YW}^{-1}x(t)$, which assigns the closed-loop poles of the system in the region $S(L_1, L_2)$ and guarantees a minimum H∞ norm γ.

C. LOAD-CURRENT FEEDFORWARD

In this section, an improved LCFF control is adopted to further enhance the dynamic response of the DAB converter, which treats the load-current as a feedforward compensation to the H∞ robust controller without impact on the design of the controller. Such an idea applied to a DAB converter with SPS control was early proposed in [11], where feedforward compensation was adopted to feed forward a phase shift correction to regulate the output voltage when the load-current changes. In this paper, a similar concept is adopted to cope with the uncertainties of the load resistance with DPS control.

To implement feedforward compensation, a relationship between the load-current and the commanded outer phase-shift ratio D_2' needs to be derived. According to the basic analysis of the DAB converter expressed in [34], the average

TABLE 2. DAB converter parameters in the HIL setup.

Symbol	Quantity	Value
P_{rated}	Converter Rated Power	5 kW
V_1	Input Voltage	250 V ~ 450 V
V_2	Output Voltage	400 V
f_s	Switching Frequency	2 kHz
D_1	Inner Phase-shift Ratio	0.2
n	Transformer Turn Ratio	5:8
L	Auxiliary Inductor Inductance	500 uH
C_1, C_2	DC Capacitance	1000 uF
$R_{\min}$, $R_{\max}$	Load Resistance	32 Ω ~ 1000 Ω

transmission power with DPS control can be rewritten as

$$P = \begin{cases} \dfrac{nV_1V_2}{2f_sL}\left[D_{2ol}^*(1 - D_{2ol}^*) - \dfrac{D_1^2}{2}\right], \\ \qquad 0 \le D_1 \le D_{2ol}^* \le 1 \\ \dfrac{nV_1V_2}{2f_sL}\left[D_{2ol}^*(1 - D_1) - \dfrac{(D_{2ol}^*)^2}{2}\right], \\ \qquad 0 \le D_{2ol}^* \le D_1 \le 1 \end{cases} \tag{23}$$

where D_{2ol}^* is an open-loop commanded outer phase-shift ratio.

Thus, the load-current can be derived as

$$I_o = \begin{cases} \dfrac{nV_1}{2f_sL}\left[D_{2ol}^*(1 - D_{2ol}^*) - \dfrac{1}{2}D_1^2\right], \\ \qquad 0 \le D_1 \le D_{2ol}^* \le 1 \\ \dfrac{nV_1}{2f_sL}D_{2ol}^*(1 - D_1 - \dfrac{1}{2}D_{2ol}^*), \\ \qquad 0 \le D_{2ol}^* \le D_1 \le 1 \end{cases} \tag{24}$$

It can be seen from (24) that the relationship between the outer phase-shift ratio and the load-current is nonlinear, resulting in complicated inverting. However, for a certain input voltage V_1, one-to-one correspondence between the ideal outer phase-shift ratio $D_{2ol}^* = D_{2FF}$ and any load-current I_o can be precalculated as lookup tables, according to the condition $0 \le D_1 \le D_{2ol}^* \le 1$ or $0 \le D_{2ol}^* \le D_1 \le 1$. Considering that the input voltage ranges from 250 V to 450 V, the lookup tables are established every 50 V for a trade-off. Moreover, for a measured input voltage within the divided interval, a linear interpolation processing is adopted to calculate the target feedforward phase-shift compensation from the two adjacent lookup tables. Thus, in every control interrupt cycle, the controller can look up and calculate the new feedforward compensation for the next control cycle. Fig. 4 shows the block diagram of LCFF compensation implemented in an H∞ robust controller of the DAB converter. According to (24), the lookup tables are calculated and presented in Table 1.

IV. EXPERIMENTAL VERIFICATION

To verify the proposed design of H∞ robust controller, a real-time hardware-in-the-loop (HIL) platform is established. The

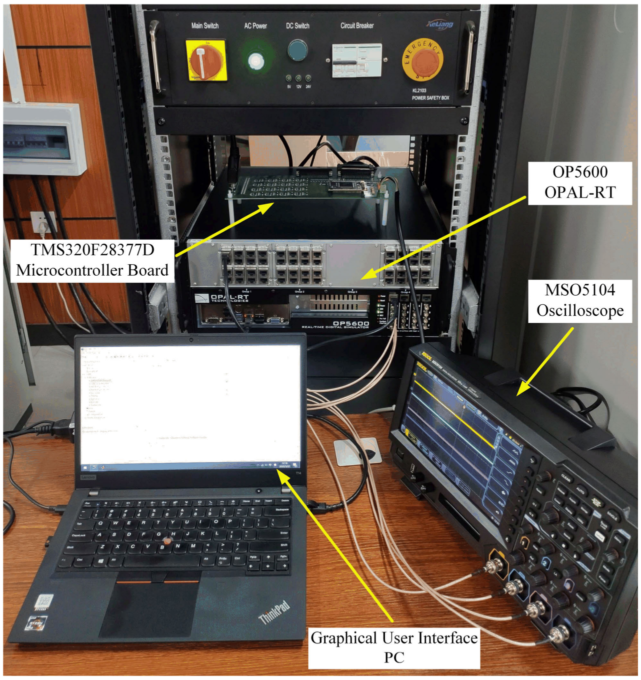

FIGURE 5. OPAL-RT real-time HIL platform with TMS320F28377D microcontroller board.

HIL setup is presented in Fig. 5, consisting of an OPAL-RT OP5600 real-time simulator and a powerful Texas Instruments TMS320F28377D Delfino microcontroller board. The DAB converter is built in the OP5600, and the proposed H∞ robust controller is implemented in the TMS320F28377D. The detailed parameters of the DAB converter in the HIL setup are presented in Table 2.

A. H∞ CONTROLLER DESIGN

The control objective of the system is to obtain a minimum H∞ norm γ by assigning the closed-loop poles within the given region $S\,(L_1, L_2)$ according to solving the optimization problem (22). In this paper, considering the minimum decay rate and the maximum natural frequency of the system, L_1 can be set to 120, while L_2 can be set to 1/20 of the switching frequency.

When the condition meets $0 \leq D_1 \leq D_2 \leq 1$, by combining the detailed parameters in Table 2, the four vertices in the polytopic model of the DAB converter shown in (16) are calculated as

$$\begin{aligned} \boldsymbol{A}_1 &= \begin{bmatrix} -1 & 0 \\ -1 & 0 \end{bmatrix}, \quad \boldsymbol{B}_{u1} = \begin{bmatrix} 46875 \\ 0 \end{bmatrix}, \\ \boldsymbol{A}_2 &= \begin{bmatrix} -31.25 & 0 \\ -1 & 0 \end{bmatrix}, \quad \boldsymbol{B}_{u2} = \begin{bmatrix} 115310 \\ 0 \end{bmatrix}, \\ \boldsymbol{A}_3 &= \boldsymbol{A}_2, \quad \boldsymbol{B}_{u3} = \boldsymbol{B}_{u1}, \\ \boldsymbol{A}_4 &= \boldsymbol{A}_1, \quad \boldsymbol{B}_{u4} = \boldsymbol{B}_{u2} \end{aligned} \tag{25}$$

Then, the remaining disturbance matrix $\boldsymbol{B}_w$ is calculated as

$$\boldsymbol{B}_w = \begin{bmatrix} -1000 \\ 0 \end{bmatrix} \tag{26}$$

Here, all the parameters and matrices used to solve the optimization problem (22) are obtained. With the help of MATLAB LMI toolbox, a total amount of fourteen LMIs can be formulated by introducing every vertex into (18), (20) and (21). The fourteen formulated LMIs consist of four LMIs from (18), four LMIs from (20), four LMIs from (21), one LMI from positive H∞ norm γ, and one LMI from positive definite matrix $\boldsymbol{W}$.

Take the LMIs of (18) for example, when the first vertex $[\boldsymbol{A}_1, \boldsymbol{B}_{u1}]$ is introduced, the corresponding formulated LMI with MATLAB commands is expressed as

```
lmiterm([1 1 1 W],A1,1,'s');
lmiterm([1 1 1 Y],Bu1,1,'s');
lmiterm([1 1 2 0],Bw);
lmiterm([1 1 3 W],1,Cz');
lmiterm([1 1 3 Y],1,Dzu');
lmiterm([1 2 2 gama],-1,1);
lmiterm([1 3 3 gama],-1,1);
```

Thus, solving the optimization problem (22) by using MATLAB LMI toolbox, a set of common matrices $\boldsymbol{Y}$ and $\boldsymbol{W}$ can be found, obtaining the H∞ controller $\boldsymbol{K}$ as

$$\boldsymbol{K} = \begin{bmatrix} K_1 & K_2 \end{bmatrix} = \begin{bmatrix} 0.0061 & 0.7969 \end{bmatrix} \tag{27}$$

and the H∞ norm is $\gamma = 6.9393$ (also known as 16.83 dB). The control law $u(t) = d_2(t) = \boldsymbol{K}x(t)$ to yield the outer phase-shift ratio can be expressed as

$$d_2(t) = 0.0061v_2(t) + 0.7969x_2(t) \tag{28}$$

Similarly, when the condition meets $0 \leq D_2 \leq D_1 \leq 1$, the control law to yield the outer phase-shift ratio can be obtained as

$$d_2(t) = 0.0071v_2(t) + 0.9491x_2(t) \tag{29}$$

B. EXPERIMENTAL RESULTS

Fig. 6 shows the steady-state experimental waveforms under the proposed H∞ robust controller when the primary side dc voltage V_1 is 250 V. It is clear that the secondary side dc voltage V_2 can be regulated at the designed 400 V under both half-load (R = 64 Ω) and full-load (R = 32 Ω). The full-bridge voltages v_p and v_s are high-frequency three-level waves with the effect of the inner phase-shift ratio, but the outer phase-shift ratio between v_p and v_s has a larger value under full-load in Fig. 6(b) compared with half-load in Fig. 6(a), due to more power needs to be transmitted under full-load.

Under the same load conditions, Fig. 7 shows the steady-state experiment waveforms under the proposed controller while the primary side dc voltage V_1 is set to 450 V. According to Fig. 7, The secondary side dc voltage V_2 is still regulated at the designed 400 V, and the outer phase-shift ratio has a larger value under full-load, while the waveforms of the auxiliary Inductor current i_L become triangle-like instead of trapezoid-like in Fig. 6, with higher peak values.

Fig. 8 shows the dynamic-state experimental comparison of the DAB converter under conventional and proposed

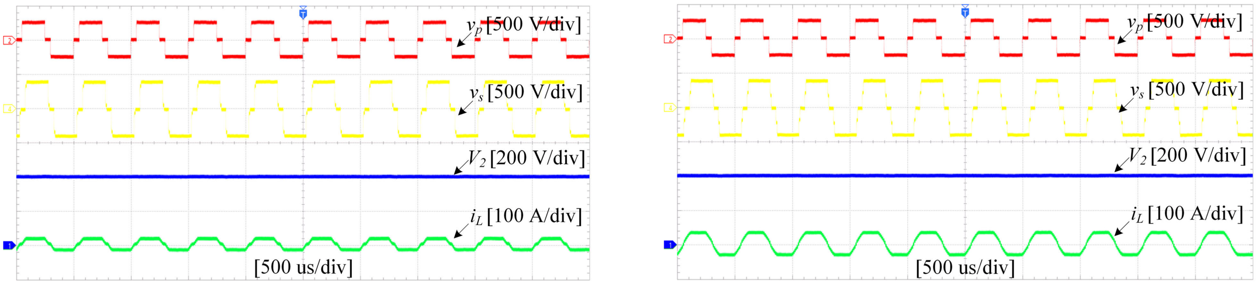

(a) (b)

FIGURE 6. Steady-state experimental waveforms of DAB converter under the proposed controller when the primary side dc voltage is 250 V: (a) Half-load (R = 64 Ω), (b) Full-load (R = 32 Ω).

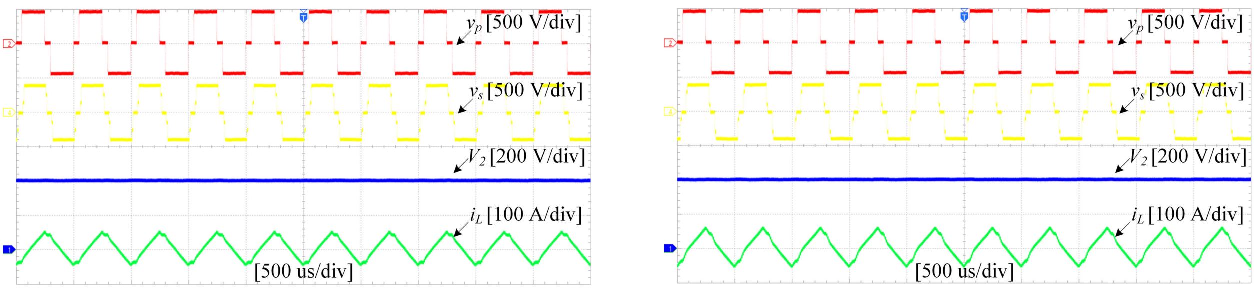

(a) (b)

FIGURE 7. Steady-state experimental waveforms of DAB converter under the proposed controller when the primary side dc voltage is 450 V: (a) Half-load (R = 64 Ω), (b) Full-load (R = 32 Ω).

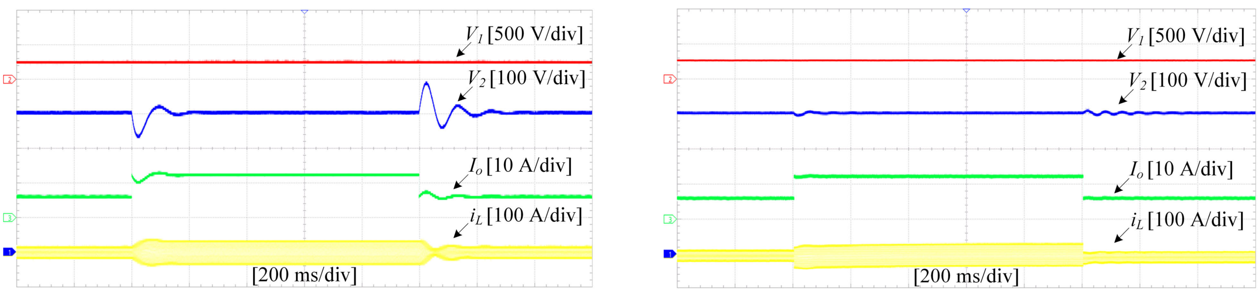

(a) (b)

FIGURE 8. Dynamic-state experimental comparison of DAB converter under conventional and proposed controllers when the primary side dc voltage is 250 V: (a) Conventional controller with load switching between half-load (R = 64 Ω) and full-load (R = 32 Ω), (b) Proposed controller with load switching between half-load (R = 64 Ω) and full-load (R = 32 Ω).

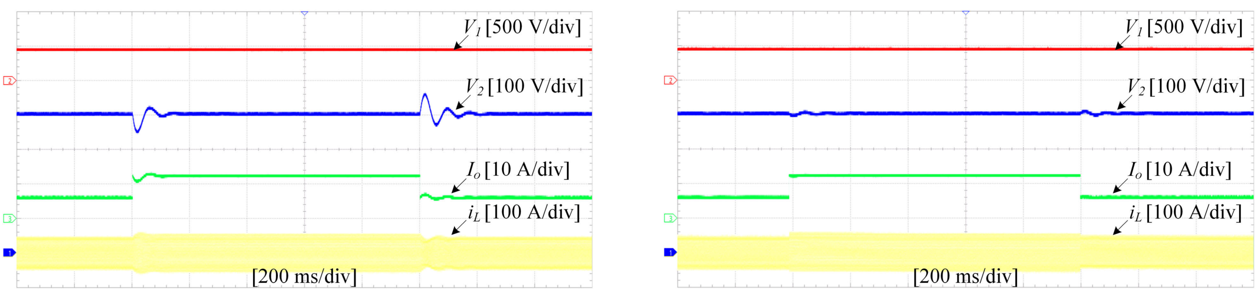

(a) (b)

FIGURE 9. Dynamic-state experimental comparison of DAB converter under conventional and proposed controllers when the primary side dc voltage is 450 V: (a) Conventional controller with load switched between half-load (R = 64 Ω) and full-load (R = 32 Ω), (b) Proposed controller with load switched between half-load (R = 64 Ω) and full-load (R = 32 Ω).

controllers when the primary side dc voltage V_1 is 250 V, and the load is switched between half-load and full-load. According to Fig. 8(a), when the load is jumped from half-load to full-load by using the conventional PI controller,

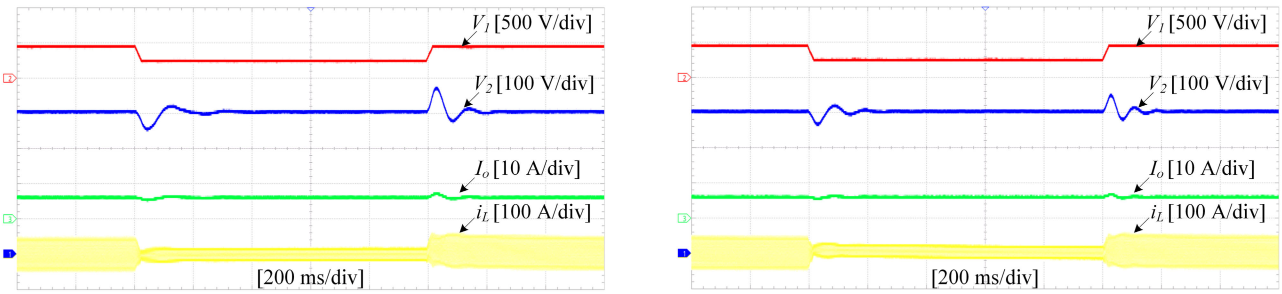

(a) (b)

FIGURE 10. Dynamic-state experimental comparison of DAB converter under conventional and proposed controllers with half-load condition (R = 64 Ω) and primary side dc voltage switching between 250 V and 450 V: (a) Conventional controller, (b) Proposed controller.

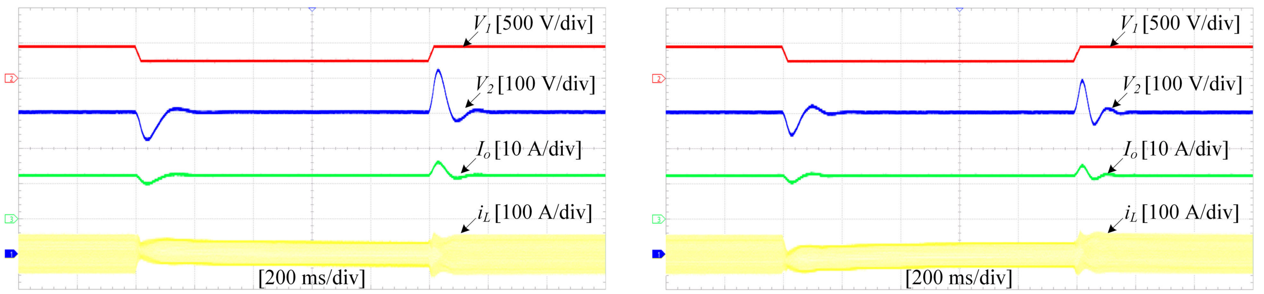

(a) (b)

FIGURE 11. Dynamic-state experimental comparison of DAB converter under conventional and proposed controllers with full-load condition (R = 32 Ω) and primary side dc voltage switching between 250 V and 450 V: (a) Conventional controller, (b) Proposed controller.

the secondary side dc voltage V_2 drops to 330 V, and the settling time takes almost 200 ms. However, as can be seen in Fig. 8(b), under the proposed controller, the experimental result shows satisfactory dynamic performances when switching between half-load and full-load, with slight voltage fluctuations and settling times.

Similar to Fig. 8, Fig. 9 shows the dynamic-state experimental comparison of the DAB converter under the conventional and proposed controllers while the primary side dc voltage V_1 is set to 450 V. As shown in Fig. 9(a), it is obvious that the secondary side dc voltage V_2 by using the conventional PI controller presents non-negligible voltage oscillations when the load varies, with a larger voltage fluctuation of 60 V and a longer settling time of 200 ms when the load is jumped from full-load to half-load. As a comparison in Fig. 9(b), the proposed controller shows excellent dynamic performances when switching between half-load and full-load, with negligible voltage fluctuations and settling times.

Fig. 10 and Fig. 11 show the dynamic-state experimental comparisons of the DAB converter under the conventional and proposed controllers with different load conditions and the change of primary side dc voltage. It can be seen that the effect of the proposed controller is mainly to reduce the amount of voltage fluctuation of the secondary side dc voltage V_2. Under the half-load condition, the voltage fluctuation of V_2 can be reduced by about 15 V when the primary side dc voltage V_1 is switched between 250 V and 450 V. Moreover, under the full-load condition, the voltage fluctuation of V_2 can be reduced by almost 20 V.

According to Fig. 8 to Fig. 11, it can be concluded that the proposed H∞ robust controller achieves better dynamic response than the conventional PI controller when load resistance jumps and primary side dc voltage variations. Furthermore, over the entire primary side dc voltage range of 250 V to 450 V, it indicates that the proposed H∞ robust controller can achieve system stability and robustness whenever half-load or full-load.

V. CONCLUSION

This paper presents the design of H∞ robust controller with load-current feed-forward for the DAB converter used in BESS. Based on DPS control, a polytopic model of the DAB converter with two uncertain elements is first established by convex optimization theory. LMIs are then used to design the H∞ robust controller conveniently to minimize the influence of disturbance on the output voltage. To ensure the dynamic performance of the system under a wide range of operating voltage conditions, a regional closed-loop pole configuration technique is properly adopted. To further enhance the dynamic response, an improved LCFF control with lookup tables for phase-shift compensation is investigated. A series of comparative experiment results obtained from a built OPAL-RT hard-ware-in-loop platform verify that the proposed H∞ robust controller achieves robust and fast dynamic performance.

As a future work, an experimental prototype with the same rated power will be designed to further verify the performance of the proposed H∞ robust controller. And the application of H∞ robust control can be extended to the DAB converter with TPS control or other power converters.

REFERENCES

[1] R. W. A. A. D. Doncker, D. M. Divan, and M. H. Kheraluwala, "A three-phase soft-switched high-power-density DC/DC converter for high-power applications," *IEEE Trans. Ind. Appl.*, vol. 27, no. 1, pp. 63–73, Jan. 1991, doi: 10.1109/28.67533.

[2] B. Zhao, Q. Song, W. Liu, and Y. Sun, "Overview of dual-active-bridge isolated bidirectional DC–DC converter for high-frequency-link power-conversion system," *IEEE Trans. Power Electron.*, vol. 29, no. 8, pp. 4091–4106, Aug. 2014, doi: 10.1109/TPEL.2013.2289913.

[3] T. Duong and S. Choi, "Deadbeat control with bivariate online parameter identification for SPS-modulated DAB converters," *IEEE Access*, vol. 10, pp. 54079–54090, 2022, doi: 10.1109/ACCESS.2022.3176428.

[4] X. Chen, J. Xu, and G. Xu, "Hybrid SPS control for ISOP dual-active-bridge converter based on modulated coupled inductor with full load range ZVS and RMS current optimization in DC transformer applications," *IEEE Access*, vol. 10, pp. 131394–131405, 2022, doi: 10.1109/ACCESS.2022.3227965.

[5] N. Hou and Y. Li, "Communication-free power management strategy for the multiple DAB-based energy storage system in islanded DC microgrid," *IEEE Trans. Power Electron.*, vol. 36, no. 4, pp. 4828–4838, Apr. 2021, doi: 10.1109/TPEL.2020.3019761.

[6] H. Akagi, S. Kinouchi, and Y. Miyazaki, "Bidirectional isolated dual-active-bridge (DAB) DC–DC converters using 1.2-kV 400-A SiC-MOSFET dual modules," *CPSS Trans. Power Electron. Appl.*, vol. 1, no. 1, pp. 33–40, Dec. 2016, doi: 10.24295/CPSSTPEA.2016.00004.

[7] K. Yu, F. Zhuo, F. Wang, X. Jiang, and Y. Gou, "MPC-based startup current shaping strategy with state-space model of DAB in DC distribution system," *IEEE J. Emerg. Sel. Topics Power Electron.*, vol. 10, no. 4, pp. 4073–4089, Aug. 2022, doi: 10.1109/JESTPE.2021.3138102.

[8] S. Park, J. W. Park, K. H. Kim, and F. Kang, "Battery energy storage system with interleaving structure of dual-active-bridge converter and non-isolated DC-to-DC converter with wide input and output voltage," *IEEE Access*, vol. 10, pp. 127205–127224, 2022, doi: 10.1109/ACCESS.2022.3226779.

[9] D. J. Almakhles, J. S. M. Ali, S. Padmanaban, M. S. Bhaskar, U. Subramaniam, and R. Sakthivel, "An original hybrid multilevel DC–AC converter using single-double source unit for medium voltage applications: Hardware implementation and investigation," *IEEE Access*, vol. 8, pp. 71291–71301, 2020, doi: 10.1109/ACCESS.2020.2986932.

[10] H. Bai, Z. Nie, and C. C. Mi, "Experimental comparison of traditional phase-shift, dual-phase-shift, and model-based control of isolated bidirectional DC–DC converters," *IEEE Trans. Power Electron.*, vol. 25, no. 6, pp. 1444–1449, Jun. 2010, doi: 10.1109/TPEL.2009.2039648.

[11] D. Segaran, D. G. Holmes, and B. P. McGrath, "Enhanced load step response for a bidirectional DC–DC converter," *IEEE Trans. Power Electron.*, vol. 28, no. 1, pp. 371–379, Jan. 2013, doi: 10.1109/TPEL.2012.2200505.

[12] W. Song, N. Hou, and M. Wu, "Virtual direct power control scheme of dual active bridge DC–DC converters for fast dynamic response," *IEEE Trans. Power Electron.*, vol. 33, no. 2, pp. 1750–1759, Feb. 2018, doi: 10.1109/TPEL.2017.2682982.

[13] W. Zhao, X. Zhang, S. Gao, and M. Ma, "Improved model-based phase-shift control for fast dynamic response of dual-active-bridge DC/DC converters," *IEEE J. Emerg. Sel. Topics Power Electron.*, vol. 9, no. 1, pp. 223–231, Feb. 2021, doi: 10.1109/JESTPE.2020.2972960.

[14] J. Sha, L. Chen, and G. Zhou, "Discrete extended-phase-shift control for dual-active-bridge DC–DC converter with fast dynamic response," *IEEE Trans. Ind. Electron.*, vol. 70, no. 6, pp. 5662–5673, Jun. 2023, doi: 10.1109/TIE.2022.3198261.

[15] T. Duong and S. Choi, "Sensor-reduction control for dual active bridge converter under dual-phase-shift modulation," *IEEE Access*, vol. 10, pp. 63020–63033, 2022, doi: 10.1109/ACCESS.2022.3182510.

[16] N. Hou, Y. Zhang, and Y. W. Li, "A load-current-estimating scheme with delay compensation for the dual-active-bridge DC–DC converter," *IEEE Trans. Power Electron.*, vol. 37, no. 3, pp. 2636–2647, Mar. 2022, doi: 10.1109/TPEL.2021.3111854.

[17] F. An, W. Song, K. Yang, N. Hou, and J. Ma, "Improved dynamic performance of dual active bridge DC–DC converters using MPC scheme," *IET Power Electron.*, vol. 11, no. 11, pp. 1756–1765, Sep. 2018, doi: 10.1049/iet-pel.2017.0707.

[18] D. Zhao, K. Shen, L. Chen, Z. Wang, W. Liu, T. Yang, and P. Wheeler, "Improved active damping stabilization of DAB converter interfaced aircraft DC microgrids using neural network-based model predictive control," *IEEE Trans. Transport. Electrific.*, vol. 8, no. 2, pp. 1541–1552, Jun. 2022, doi: 10.1109/TTE.2021.3094757.

[19] X. Meng, Y. Jia, Q. Xu, C. Ren, X. Han, and P. Wang, "A novel intelligent nonlinear controller for dual active bridge converter with constant power loads," *IEEE Trans. Ind. Electron.*, vol. 70, no. 3, pp. 2887–2896, Mar. 2023, doi: 10.1109/TIE.2022.3170608.

[20] Y. Zeng, A. I. Maswood, J. Pou, X. Zhang, Z. Li, C. Sun, S. Mukherjee, A. K. Gupta, and J. Dong, "Active disturbance rejection control using artificial neural network for dual-active-bridge-based energy storage system," *IEEE J. Emerg. Sel. Topics Power Electron.*, vol. 11, no. 1, pp. 301–311, Feb. 2023, doi: 10.1109/JESTPE.2021.3138341.

[21] L. Chen, S. Shao, Q. Xiao, L. Tarisciotti, P. W. Wheeler, and T. Dragicevic, "Model predictive control for dual-active-bridge converters supplying pulsed power loads in naval DC micro-grids," *IEEE Trans. Power Electron.*, vol. 35, no. 2, pp. 1957–1966, Feb. 2020, doi: 10.1109/TPEL.2019.2917450.

[22] L. Chen, L. Lin, S. Shao, F. Gao, Z. Wang, P. W. Wheeler, and T. Dragicevic, "Moving discretized control set model-predictive control for dual-active bridge with the triple-phase shift," *IEEE Trans. Power Electron.*, vol. 35, no. 8, pp. 8624–8637, Aug. 2020, doi: 10.1109/TPEL.2019.2962838.

[23] Y. Jeung and D. Lee, "Voltage and current regulations of bidirectional isolated dual-active-bridge DC–DC converters based on a double-integral sliding mode control," *IEEE Trans. Power Electron.*, vol. 34, no. 7, pp. 6937–6946, Jul. 2019, doi: 10.1109/TPEL.2018.2873834.

[24] N. Tiwary, V. Naik N, A. K. Panda, A. Narendra, and R. K. Lenka, "A robust voltage control of DAB converter with super-twisting sliding mode approach," *IEEE J. Emerg. Sel. Topics Ind. Electron.*, vol. 4, no. 1, pp. 288–298, Jan. 2023, doi: 10.1109/JESTIE.2022.3227007.

[25] P.-J. Ko and M.-C. Tsai, "H_∞ control design of PID-like controller for speed drive systems," *IEEE Access*, vol. 6, pp. 36711–36722, 2018, doi: 10.1109/ACCESS.2018.2851284.

[26] M. Yang, Y. Li, H. Du, C. Li, and Z. He, "Hierarchical multiobjective H-infinity robust control design for wireless power transfer system using genetic algorithm," *IEEE Trans. Control Syst. Technol.*, vol. 27, no. 4, pp. 1753–1761, Jul. 2019, doi: 10.1109/TCST.2018.2814589.

[27] L. Li, G. Pei, J. Liu, P. Du, L. Pei, and C. Zhong, "2-DOF robust H_∞ control for permanent magnet synchronous motor with disturbance observer," *IEEE Trans. Power Electron.*, vol. 36, no. 3, pp. 3462–3472, Mar. 2021, doi: 10.1109/TPEL.2020.3015874.

[28] Y. Liang, P. Sun, X. Wu, H. Zhou, J. Sun, G. Yang, J. Cai, and Q. Deng, "H_∞ robust control for ICPT system with selected weighting function considering parameter perturbations," *IEEE Trans. Power Electron.*, vol. 37, no. 11, pp. 13914–13929, Nov. 2022, doi: 10.1109/TPEL.2022.3179979.

[29] H. Ren and L. Ma, "H-infinity mixed sensitivity control of dual active bridge DC–DC converter," in *Proc. IEEE Int. Conf. Power, Intell. Comput. Syst. (ICPICS)*, Jul. 2021, pp. 16–20, doi: 10.1109/ICPICS52425.2021.9524165.

[30] C. Olalla, R. Leyva, A. E. Aroudi, P. Garces, and I. Queinnec, "LMI robust control design for boost PWM converters," *IET Power Electron.*, vol. 3, no. 1, pp. 75–85, Jan. 2010, doi: 10.1049/iet-pel.2008.0271.

[31] P. Xia, H. Shi, H. Wen, Q. Bu, Y. Hu, and Y. Yang, "Robust LMI-LQR control for dual-active-bridge DC–DC converters with high parameter uncertainties," *IEEE Trans. Transport. Electrific.*, vol. 6, no. 1, pp. 131–145, Mar. 2020, doi: 10.1109/TTE.2020.2975313.

[32] Q. Xiao, L. Chen, H. Jia, P. W. Wheeler, and T. Dragicevic, "Model predictive control for dual active bridge in naval DC microgrids supplying pulsed power loads featuring fast transition and online transformer current minimization," *IEEE Trans. Ind. Electron.*, vol. 67, no. 6, pp. 5197–5203, Jun. 2020, doi: 10.1109/TIE.2019.2934070.

[33] H. Bai and C. Mi, "Eliminate reactive power and increase system efficiency of isolated bidirectional dual-active-bridge DC–DC converters using novel dual-phase-shift control," *IEEE Trans. Power Electron.*, vol. 23, no. 6, pp. 2905–2914, Nov. 2008, doi: 10.1109/TPEL.2008.2005103.

[34] B. Zhao, Q. Song, W. Liu, and W. Sun, "Current-stress-optimized switching strategy of isolated bidirectional DC–DC converter with dual-phase-shift control," *IEEE Trans. Ind. Electron.*, vol. 60, no. 10, pp. 4458–4467, Oct. 2013, doi: 10.1109/TIE.2012.2210374.

[35] B. Zhao, Q. Song, and W. Liu, "Efficiency characterization and optimization of isolated bidirectional DC–DC converter based on dual-phase-shift control for DC distribution application," *IEEE Trans. Power Electron.*, vol. 28, no. 4, pp. 1711–1727, Apr. 2013, doi: 10.1109/TPEL.2012.2210563.

[36] F. An, W. Song, B. Yu, and K. Yang, "Model predictive control with power self-balancing of the output parallel DAB DC–DC converters in power electronic traction transformer," *IEEE J. Emerg. Sel. Topics Power Electron.*, vol. 6, no. 4, pp. 1806–1818, Dec. 2018, doi: 10.1109/JESTPE.2018.2823364.

[37] J. Bernussou, P. L. D. Peres, and J. C. Geromel, "A linear programming oriented procedure for quadratic stabilization of uncertain systems," *Syst. Control Lett.*, vol. 13, no. 1, pp. 65–72, Jul. 1989, doi: 10.1016/0167-6911(89)90022-4.

[38] S. Boyd, L. Ghaoui, E. Feron, and V. Balakrishnan, *Linear Matrix Inequality in Systems and Control Theory*. Philadelphia, PA, USA: SIAM Studies in Applied Mathematics, 1991.

[39] P. Gahinet and P. Apkarian, "A linear matrix inequality approach to H_∞ control," *Int. J. Robust Nonlinear Control*, vol. 4, no. 4, pp. 421–448, 1994, doi: 10.1002/rnc.4590040403.

[40] M. Chilali and P. Gahinet, "H_∞ design with pole placement constraints: An LMI approach," *IEEE Trans. Autom. Control*, vol. 41, no. 3, pp. 358–367, Mar. 1996, doi: 10.1109/9.486637.

XIAODONG XU was born in Gansu, China, in 1983. He received the B.S. and M.S. degrees from Xi'an Jiaotong University, Xi'an, China, in 2006 and 2010, respectively. He is currently pursuing the Ph.D. degree with the College of Electrical and Information Engineering, Lanzhou University of Technology, Lanzhou, China. Since 2012, he has been a Lecturer with the College of Energy and Power Engineering, Lanzhou University of Technology. His current research interests include pulse width modulation techniques and DC–DC converters.

GUANGQING BAO was born in China, in 1972. She received the Ph.D. degree in electrical engineering from Shanghai University, Shanghai, China, in 2006. She is currently a Professor with the School of Electrical Engineering and Information, Southwest Petroleum University, Chengdu, China. Her current research interests include special motor design, the integration of renewable energy into power systems, microgrid control and management, and renewable energy grid-connected control.

YUEWU WANG was born in Guangxi, China, in 1983. He received the Ph.D. degree in electrical engineering from the South China University of Technology, Guangzhou, China, in 2017. From 2017 to 2020, he was a Software Engineer with Shenzhen INVT Electric Company Ltd., Shenzhen, China. In 2020, he joined the School of Automation, Guangxi University of Science and Technology, Liuzhou, China, where he is currently a Lecturer. His current research interests include pulse width modulation techniques, DC–DC converters, and grid-connected inverters.

QIAN LI was born in China, in 1988. She received the Ph.D. degree in electrical engineering from Sichuan University, Chengdu, China. She is currently an Associate Professor with the School of Electrical Engineering and Information, Southwest Petroleum University, Chengdu. Her current research interests include power system stability and control, distributed generation, and integrated energy systems.

Original scientific paper

https://doi.org/10.33180/InfMIDEM2021.303

Informacije MIDEM
Journal of Microelectronics, Electronic Components and Materials
Vol. 51, No. 3(2021), 169 – 179

Multi-Objective Optimization Phase-Shift Control Strategy for Dual-Active-Bridge Isolated Bidirectional DC-DC Converter

Xiaodong Xu[1], Guangqing Bao[1], Ming Ma[2], Yuewu Wang[3]

[1]*College of Electrical and Information Engineering, Lanzhou University of Technology, Lanzhou, China*
[2]*Wind Power Technology Center, State Grid Gansu Electric Power Corporation, Lanzhou, China*
[3]*School of Electrical Engineering and Automation, Harbin Institute of Technology, Harbin, China*

Abstract: The dual-active-bridge isolated bidirectional DC-DC converter (DAB-IBDC) is a crucial device for galvanic isolation, voltage conversion, power transfer, and bus connection in the DC power conversion systems. Phase-shift modulation is an effective method to improve DAB-IBDC performance. However, the phase-shift control strategies in the previous literatures mainly focus on optimizing the characteristic of DAB-IBDC in a single aspect. In this paper, to optimize high-frequency-link (HFL) reactive power, current stress, and efficiency simultaneously, a new multi-objective optimization strategy based on dual-phase-shift (DPS) control is proposed. The power characterization, current stress, and power loss of the DAB-IBDC are analyzed. Besides, both the control principle and framework of the proposed control strategy are described in detail. Finally, the experiment results obtained from an established DAB-IBDC prototype are presented to verify the correctness and superiority of the proposed strategy.

Keywords: dual-active-bridge; multi-objective optimization; DPS control strategy; electrical performance

Strategija upravljanja faznega premika z več ciljnimi optimizacijami za dvoaktivni izolirani mostič dvosmernega DC-DC pretvornika

Izvleček: Izolirani dvosmerni DC-DC (DAB-IBDC) pretvornik z dvoaktivnim mostičem je ključna naprava za galvansko izolacijo, pretvorbo napetosti, prenos moči in povezavo vodila v sistemih za pretvorbo enosmerne energije. Modulacija s faznim zamikom je učinkovita metoda za izboljšanje delovanja DAB-IBDC. Vendar se strategije nadzora s faznim zamikom v dosedanji literaturi osredotočajo predvsem na optimizacijo značilnosti DAB-IBDC z enega vidika. V tem članku je za hkratno optimizacijo jalove moči, tokovne napetosti in učinkovitosti visokofrekvenčne povezave (HFL) predlagana nova večpredmetna strategija optimizacije, ki temelji na nadzoru z dvojnim faznim zamikom (DPS). Analizirane so značilnosti moči, tokovne obremenitve in izgube moči DAB-IBDC. Poleg tega sta podrobno opisana tako načelo krmiljenja kot tudi okvir predlagane strategije krmiljenja. Na koncu so predstavljeni rezultati poskusov, pridobljeni iz vzpostavljenega prototipa DAB-IBDC, s katerimi sta preverjeni pravilnost in superiornost predlagane strategije.

Ključne besede: dvojni aktivni mostič; večnamenska optimizacija; strategija krmiljenja DPS; električna zmogljivost

** Corresponding Author's e-mail: gqbao@lut.cn*

1 Introduction

With the wide application of direct-current (DC) renewable power sources, DC loads, and storage equipment, DC power conversion systems (PCS) have considerable potential for engineering applications [1-4]. With the development of power electronics, isolated bidirectional DC-DC converters (IBDCs) have become popular for galvanic isolation, voltage conversion, and power transfer in DC PCS [5-6]. Among various IBDCs, the du-

How to cite:
X. Xu et al.,"Multi-Objective Optimization Phase-Shift Control Strategy for Dual-Active-Bridge Isolated Bidirectional DC-DC Converter", Inf. Midem-J. Microelectron. Electron. Compon. Mater., Vol. 51, No. 3(2021), pp. 169–179

al-active-bridge (DAB) IBDC with merits of symmetric topology and control structure, the convenience of implement zero voltage switching for switches, bidirectional power transmission, and cascaded modularity, has been studied and applied in the DC PCS. Thanks to the development of novel power devices and technologies, the DAB-IBDC performance is greatly improved under the great efforts of researchers and engineers. The improvements in DAB-IBDC also promote the development of PCS, so bringing lots of technical advantages [7-10].

The improvements of DAB-IBDC in the previous literatures mainly focus on the topology design and optimization, mathematical model derivation, phase-shift modulation strategies, converter control schemes, and soft-switching realization [11-15]. Particularly, the phase-shift control is an effective method to optimize the DAB-IBDC performance [16]. The phase-shift control strategies can be categorized into single-phase-shift (SPS), extended-phase-shift (EPS), dual-phase-shift (DPS), and triple-phase-shift (TPS). With DAB configurations each full bridge is driven with specific phase-shift. While these phase-shifts can differ in DPS they are equal and referred as inner phase-shift, and phase-shift between each full bridge is the outer phase-shift [7]. The SPS has one degree of freedom with outer phase-shift, and the EPS and DPS have two degrees of freedom with inner phase-shift and outer phase-shift, while the TPS has three degrees of freedom with two different inner phase-shifts and an outer phase-shift. In [17], an improved asymmetric modulation for both-side of DAB-IBDC is proposed, enabling the smooth transaction during steady-state operation and minimizing the transient time regardless of equivalent resistance of inductor. In [18], optimized phase-shift modulations are proposed to accelerate the transient response and suppress the DC bias during transient process. In [19-20], a mathematical model of current stress for DAB-IBDC is established, and the minimum current stresses are achieved under DPS and TPS control strategies, respectively. In [21-22], the DAB-IBDCs with soft-switching operation during whole operating range are analyzed, expanding the zero-voltage switching (ZVS) range and promoting efficiency. In [23-24], the power loss and efficiency models are established, and the efficiency optimized modulation schemes based on phase-shift control are developed. Other phase-shift modulation strategies are also proposed in [25-28] to eliminate reactive power, reduce the peak and root-mean-square (RMS) values of HFL current, and enhance light-load performance for DAB-IBDC, respectively. Moreover, the phase-shift strategies with quasi-square-wave, triangle-wave and sine-wave modulation are investigated for improving performance under varied modulation methods [29-30]. Besides, the TPS control strategy is an efficient method to improve the performance of DAB [31-33].

The phase-shift control strategies in the previous literatures have improved the performance of DAB-IBDC effectively. However, most existing phase-shift control strategies only realize the performance optimization in a single aspect (e.g., current stress, reactive power elimination, ZVS behavior, or efficiency performance of DAB-IBDC). The phase-shift control strategy for multi-objective optimization, i.e., simultaneously optimizes various characteristics of DAB-IBDC, has not been considered and discussed yet. Besides, some phase-shift control strategies with optimal phase-shift angle contain lots of electrical parameters, nonlinear equations, or trigonometric calculation, leading to a high computational burden, a complicated process, and a poor real-time characteristic in practical application. In this paper, to address the above problems and achieve the comprehensive optimization for DAB-IBDC, a multi-objective optimization strategy with DPS control is proposed. The proposed strategy can reduce current stress, improve transmission power, and minimize power loss simultaneously. Consequently, the proposed strategy can achieve high efficiency and improve adaptability and practicality for DAB-IBDC, which promotes the application of DAB-IBDC and also accelerates the development of DC PCS.

This paper is organized as follows. The topology, switching behavior based on DPS control, and the performance characteristics including the high-frequency-link (HFL) current stress, power factor, and power loss of the DAB-IBDC are investigated in Section 2. On this basis, a multi-objective optimization based on DPS control is proposed in Section 3. Then, Section 4 provides the experimental results obtained from a built DAB-IBDC prototype to verify the proposed strategy.

2 Performance characteristics of DAB-IBDC under DPS control

The topology of the DAB-IBDC is presented in Fig. 1. The DAB-IBDC is consisted of active full-bridges H_1 and H_2, two DC capacitors C_1 and C_2, an auxiliary inductor L_T and an high-frequency-link (HFL) transformer with a conversion ratio n. $S_1 \sim S_4$ and $D_1 \sim D_4$ are switches and diodes in H_1, respectively, and $Q_1 \sim Q_4$ and $M_1 \sim M_4$ are switches and diodes in H_2, respectively. V_1 and V_2 are DC voltages on two sides of DAB-IBDC, respectively. The energy transfer could be equivalent to the transmission of energy between two modulated voltage sources through equivalent inductor L. i_L is HFL current flowing through the equivalent inductor. v_P is the HFL voltage on the primary side. v_s is the HFL voltage on the secondary side, which is generated by secondary terminate and equivalent to the primary-side voltage.

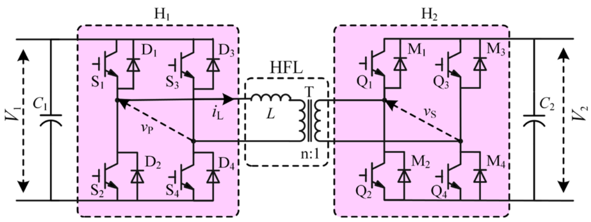

Figure 1: Topology configuration of DAB-IBDC.

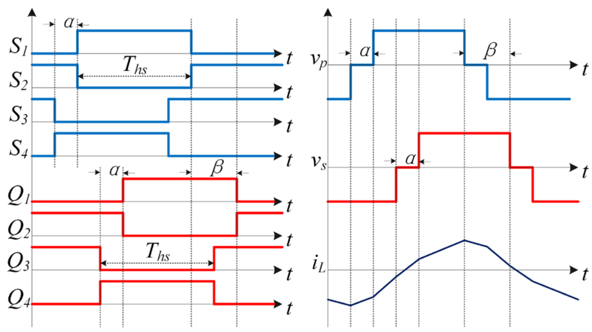

Figure 2: The operation principle, HFL voltages, and currents under DPS control.

Generally, the DPS control has two working modes: the inner phase-shift ratio is larger or smaller than the outer phase-shift ratio, which is determined by the transferred power [7]. Different from EPS and TPS, the inner phase-shift ratios under DPS strategy in active full-bridges on both sides are the same. T_s is the switching period. To avoid the analysis complexity brought from the traditional time-domain segmentation function, the unified model form based on the Fourier series is applied in the analysis and control design. According to the topology of DAB-IBDC, the operation principle, HFL voltages, and currents under DPS control are presented in Fig. 2, where β is the outer phase-shift angle between v_p and v_s, and $\alpha_1 = \alpha_2 = \alpha$ is the inner phase-shift angle.

According to Fourier series, the primary and secondary side HFL voltages v_p and v_s, shown in Fig. 2, are:

$$\begin{cases} v_p(t) = \sum\limits_{k=1,3,5...} \dfrac{4V_1}{k\pi}\cos(\dfrac{k\alpha}{2})\sin(n\omega t) \\ v_s(t) = \sum\limits_{k=1,3,5...} \dfrac{4V_2}{k\pi}\cos(\dfrac{k\alpha}{2})\sin[n(\omega t-\beta)] \end{cases} \tag{1}$$

Since the average inductor current is equal to zero during steady-state, the HFL current i_L in every switching period can be express as:

$$i_L(t) = \int_{t_0}^{t} \frac{v_P(t)-v_S(t)}{L}dt + i_L(t_0) \tag{2}$$

From (1) - (2), the following equations can be obtained:

$$\begin{cases} i_L(t) = \sum\limits_{k=1,3,5...} \dfrac{4}{k^2\pi\omega L}\sqrt{A^2+B^2}\sin(k\omega t+\arctan\dfrac{A}{B}) \\ A = \cos(\dfrac{k\alpha}{2})[V_2\cos(k\beta)-V_1] \\ B = V_2\cos(\dfrac{k\alpha}{2})\sin(k\beta) \end{cases} \tag{3}$$

Thus, the root-mean-square (RMS) value of i_L is:

$$I_{L-RMS} = \sqrt{\sum_{k=1,3,5...} I_{Lk}{}^2} = \sqrt{\sum_{k=1,3,5...} [\frac{2\sqrt{2}}{k^2\pi\omega L}\sqrt{A^2+B^2}]^2} \tag{4}$$

2.1 Transmission power characterization

The average transmission power P can be obtained as:

$$P = \frac{1}{T_{hs}}\int_0^{T_{hs}} v_p(t)\bullet i_L(t)dt \tag{5}$$

Substituting (1) - (3) into (5), the average transmission power P can be further calculated as:

$$P = \sum_{k=1,3,5...} \frac{8V_1V_2}{k^3\pi^2\omega L}\cos^2(\frac{k\alpha}{2})\sin(k\beta) \tag{6}$$

Besides, the reactive power Q can be obtained:

$$\begin{cases} Q_{k_1=k_2=k} = \sum\limits_{k=1,3,5...} \dfrac{8V_1\cos^2(\dfrac{k\alpha}{2})}{k^3\pi^2\omega L}[V_1-V_2\cos(k\beta)] \\ Q_{k_1\neq k_2} = U_{ak_1}I_{Lk_2} = \dfrac{8V_1}{k_1k_2^2\pi^2\omega L}\cos(\dfrac{k\alpha}{2})\sqrt{A^2+B^2} \end{cases} \tag{7}$$

From (6) - (7), the apparent power S is calculated as:

$$S = \sqrt{\sum_{k=1,3,5...} P_k^2 + \sum_{k=1,3,5...} Q_k^2 + \sum_{k=1,3,5...} Q_{k_1\neq k_2}^2} \tag{8}$$

Finally, the HFL power factor λ can be obtained as:

$$\lambda = P/S \tag{9}$$

Based on (6) - (9), Fig. 3 shows the HFL power factors under conventional control strategy. In Fig. 3, the HFL power factor λ is influenced by phase-shift angles, and the HFL power factors under DPS are higher. Besides, under DPS ($DPS_1 < DPS_2 < DPS_3$), with the increasing of inner angle α, the HFL power factor λ becomes higher correspondingly, decreasing HFL reactive power and increasing efficiency of DAB-IBDC.

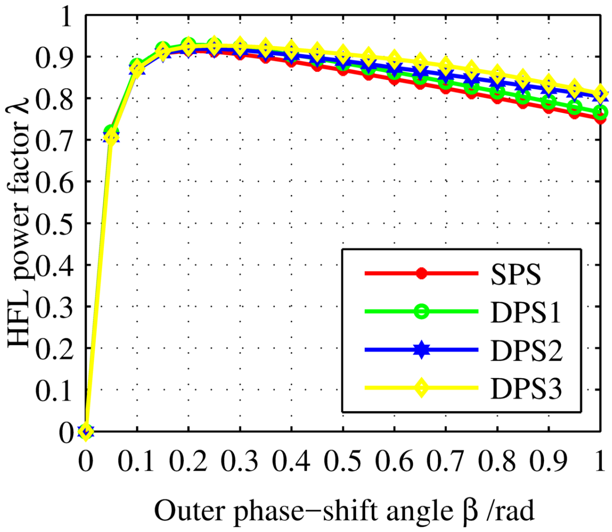

Figure 3: HFL power factors of DAB-IBDC.

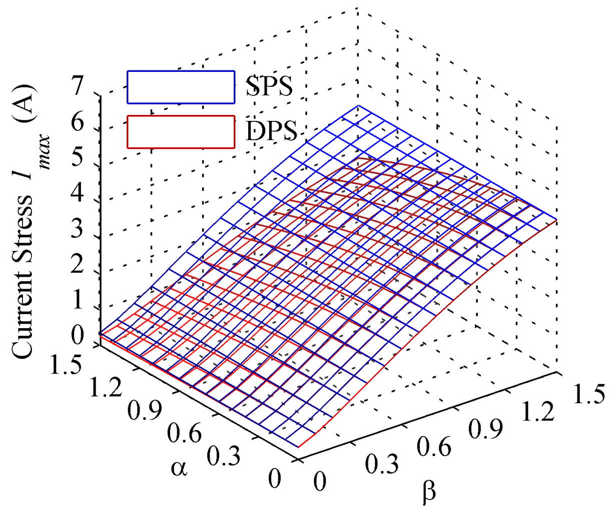

Figure 4: The current stress of DAB-IBDC.

2.2 Current stress characterization

To prolong the service life of switching devices, and improve the efficiency of DAB-IBDC, reducing the current stress is an effective solution. In the DAB-IBDC, the maximum value of HFL current i_L represents the current stress. From (3), it can be observed that the HFL current i_L compromises components with different frequencies under Fourier series analysis. Since the fundamental component in HFL current i_{L1} is approximated with HFL current i_L during operation, the maximum value of the fundamental component of i_L can be considered as the current stress I_{max}:

$$I_{max} = \max\{|i_{L1}(t)|\} = \frac{2V_2\cos(\frac{\alpha}{2})\sqrt{1+M^2-2M\cos(\beta)}}{\pi\omega L} \quad (10)$$

where $M = V_1 / nV_2$ is the voltage conversion ratio of DAB-IBDC.

According to (10), the current stress is closely related to V_1, V_2, α, β, and M. Fig. 4 presents the current stress I_{max} with the different α and β under the SPS and DPS control. From Fig. 4, it can be observed: 1) with the increase of outer β, the current stress I_{max} increases under these two strategies, 2) under the same outer β, the current stress produced by DPS control is kept smaller. Besides, the current stress can be reduced with the increase of phase-shift α under DPS.

2.3 Power loss characterization

For DAB-IBDC, its total power loss P_{LOSS} mainly contains conducting loss P_{CON}, switching loss P_{SW}, and loss of magnetic components P_{TA} [24].

$$P_{LOSS} = P_{CON} + P_{SW} + P_{TA} \quad (11)$$

(1) Conducting loss: From the topology of DAB-IBDC, the conducting loss P_{CON} is the sum of conducting losses in switches and diodes namely P_{CONS} and P_{COND}, respectively. For the DAB-IBDC, the dead-band loss should be considered and could not be ignored. As the zero-voltage-switching (ZVS) for DAB-IBDC can be also realized by using the freewheeling of anti-parallel diodes during dead-band time. Thus, the dead-band current is freewheeling in diodes, which means the dead-band loss can be considered as a part of conducting loss. For simplicity, assume that the diodes and switches in DAB-IBDC have the same conducting resistance R_{CON}. Besides, the conducting loss is closely related to the RMS HFL current in primary bridge H_1 and secondary bridge H_2 namely I_1 and I_2, respectively. The relationship between I_1 and I_2 is $I_1 = I_2 / n = I / \sqrt{2}$. Consequently, the conducting loss of switches and diodes in a switching period are:

$$P_{CON} = 4R_{CON}I_1^2 + 4R_{CON}I_2^2 = 2(1+n^2)R_{CON}I_{L\text{-}RMS}^2 \quad (12)$$

Based on (12), the conduction losses P_{CON} is mainly decided by RMS current $I_{L\text{-}RMS}$ of HFL. Under both SPS and DPS control, the conduction loss P_{CON} for DAB-IBDC are presented in Fig. 5(a), and they are normalized by $P_{CON} = 2(1 + n^2) R_{CON} I_{L\text{-}max}^2$. Obviously, with the increase of phase-shift angle β, the conduction loss P_{CON} increases, while P_{CON} under DPS is always smaller. Besides, the conduction loss P_{CON} drops with the increase of inner phase-shift α.

(2) Switching loss: From [24], with the same transfer power, switching loss is relatively smaller compared with the conducting loss and the loss of magnetic components, and it only accounts for a small proportion of the overall power loss of DAB-IBDC. Besides, under soft-switching achievement, the switching loss can be neglected. Thus, for simplicity, the switching loss is ignored here.

(3) Loss of magnetic components: In DAB-IBDC, magnetic components include the transformer and the auxiliary inductor. Typically, the power loss of magnetic component consists of the copper loss and core loss. Assuming that the winding resistance of magnetic components is constant, the copper loss P_{COPP} is closely related to the RMS value of i_L. In addition, the RMS value of i_L also plays a major role in the core loss P_{CORE}. The power loss of magnetic components P_{TA} can be obtained as:

$$P_{\mathrm{TA}} = P_{\mathrm{COPP}} + P_{\mathrm{CORE}} = (R_{\mathrm{tr}} + R_{\mathrm{au}} + \frac{2mf_s\mu_0^2 N^2 V_e}{g^2})I_{\mathrm{L\text{-}RMS}}^2 \tag{13}$$

where R_{tr} is the transformer winding resistance while R_{au} is auxiliary inductor winding resistance. m represents the specific parameter of core loss, μ_0 represents the permeability of vacuum, N represents the number of turns, V_e represents the effective core volume, and g represents the air gap of magnetic path.

Based on (13), the power loss P_{TA} is affected by the RMS current $I_{L\text{-}RMS}$ of HFL. Fig. 5(b) shows the curves of normalized power loss of magnetic components P_{TA} for DAB-IBDC under DPS, in which they are normalized by $P_{TA} = (R_{tr}+R_{au}+2mf_s u_0^2N^2V_e/g_2)I_{L\text{-}max}^2$. It is obvious that, the power loss P_{TA} increases with the raise of outer angle β, which is smaller under DPS compared with SPS. Besides, the P_{TA} reduces with the raise of the inner angle α.

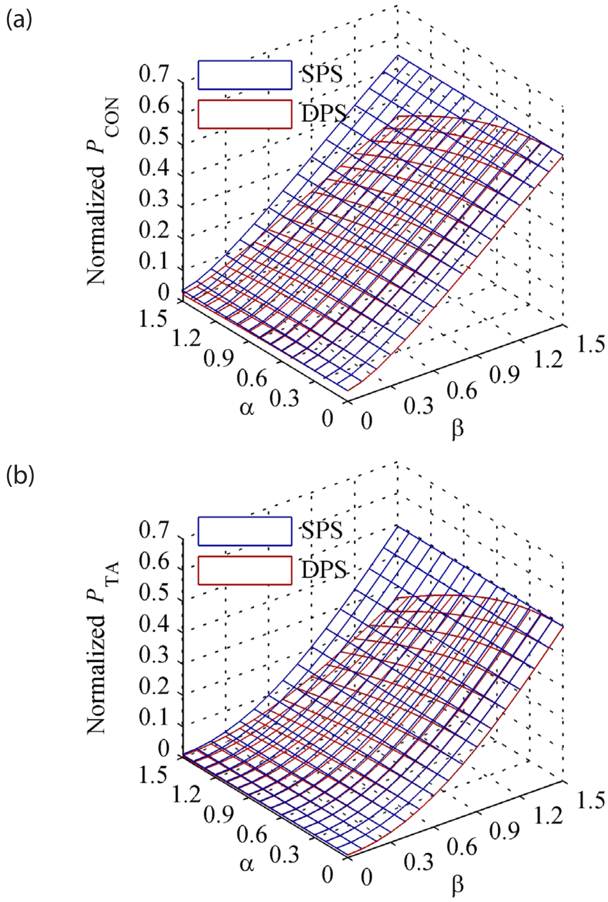

Figure 5: The power loss for DAB-IBDC. (a) Conducting loss, (b) Loss of magnetic components.

3 Multi-objective optimized strategy based on DPS control

From the analysis above, in the DAB-IBDC, all the HFL reactive power, current stress, and efficiency performance could be optimized by DPS strategy simultaneously. Accordingly, an optimized strategy based on DPS control is investigated for DAB-IBDC.

The current stress I_{max}, conducting loss P_{CON}, and loss of magnetic components P_{TA} are:

$$\begin{cases} I_{\max} = I_L = \sqrt{2} I_{\mathrm{L\text{-}RMS}} \\ P_{\mathrm{con}} = 2(1+n^2) R_{\mathrm{CON}} I_{\mathrm{L\text{-}RMS}}^2 \\ P_{\mathrm{TA}} = (R_{\mathrm{tr}} + R_{au} + \frac{2mf_s\mu_0^2 N^2 V_e}{g^2}) I_{\mathrm{L\text{-}RMS}}^2 \end{cases} \tag{14}$$

From (14), it could be seen that the current stress of DAB-IBDC is affected by the RMS value of HFL current $I_{L\text{-}RMS}$. Besides, the conducting loss P_{CON} and loss of magnetic components P_{TA} are also mainly affected by the RMS current of HFL. Thus, through optimizing the HFL current, the current stress, power loss, and the efficiency can be all optimized. Once the optimal RMS value of HFL current is obtained, the optimization of current stress and efficiency for DAB-IBDC could be realized at the same time.

To obtain the optimal RMS value of HFL current, a Lagrangian objective function is constructed:

$$E(\alpha,\beta,\lambda) = I_{\mathrm{L\text{-}RMS}}(\alpha,\beta) + \lambda(P(\alpha,\beta) - P_0) \tag{15}$$

where P_0 is the calculated output power for DAB-IBDC, which is obtained through multiplying the reference output voltage V_{2ref} by the output current I_2. Substituting (6) and (10) into (15), the constraints of the optimal equation can be obtained as:

$$\begin{cases} E = \dfrac{2nV_2\cos(\frac{\alpha}{2})\sqrt{1+M^2-2M\cos(\beta)}}{\pi\omega L} + \\ \quad \lambda[\dfrac{4V_1V_2 n}{\pi^2\omega L}\cos^2(\frac{\alpha}{2})\sin(\beta) - P_0] \\ \dfrac{\partial E}{\partial \alpha} = \sqrt{1+M^2-2M\cos(\beta)} + \dfrac{4\lambda V_1}{\pi}\cos(\frac{\alpha}{2})\sin(\beta) = 0 \\ \dfrac{\partial E}{\partial \beta} = \dfrac{M\sin(\beta)}{\sqrt{1+M^2-2M\cos(\beta)}} + \dfrac{2\lambda V_1}{\pi}\cos(\frac{\alpha}{2})\cos(\beta) = 0 \\ \dfrac{\partial E}{\partial \lambda} = \dfrac{4V_1V_2 n}{\pi^2\omega L}\cos^2(\frac{\alpha}{2})\sin(\beta) - P_0 = 0 \end{cases} \tag{16}$$

From (15) and (16), the optimal solution (α, β) for DAB-IBDC under DPS control can be obtained by the results of the nonlinear equations in (16), and the DPS-based optimized strategy for DAB-IBDC is presented in Fig. 6. For the proposed strategy, the outer angle β is obtained from the output voltage control loop. An optimized calculation model is used to obtain the inner angle α for reducing the current stress/power loss and improving the efficiency of DAB-IBDC.

From (16), the common solution and Pareto front of optimization for inner angle α is further obtained:

$$\alpha = \arccos\sqrt{\frac{P_0\pi^2\omega L}{nV_1V_2\sin(\beta)}} \tag{17}$$

From (17), since the fluctuations in switching frequency and inductance value are very small compared with the magnitude of normalized transmission power and DC voltages, their influence on optimization result will be very small. Therefore, the optimal inner phase-shift angle α is mainly determined by outer phase-shift angle β, relatively fixed parameters normalized transmission power P_o, the HFL voltage ratio n, and also DC voltages V_1 and V_2.

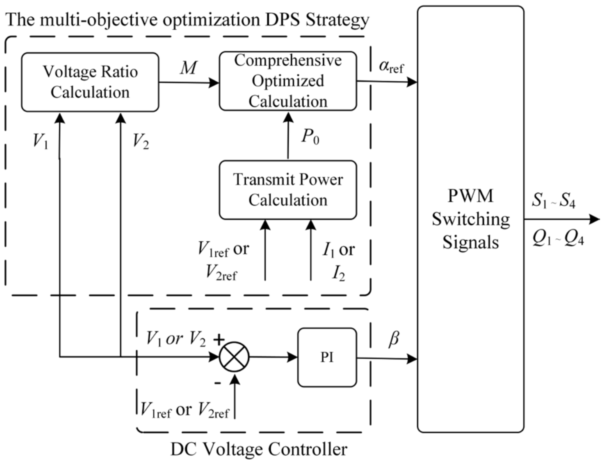

Figure 6: Control framework of proposed multi-objective optimized DPS strategy for DAB-IBDC.

4 Experiment verification

To verify the proposed control strategy, a 1kW rated DAB-IBDC prototype is established, and the load power rating is rated 1kW. The detailed parameters are presented in Table 1, and the prototype is shown in Fig. 7.

Table 1: Parameters of DAB-IBDC Prototype.

Parameters	Value	Symbol
Primary Side DC Voltage	50V ~ 150V	V_1
Secondary Side DC Voltage	50V ~ 150V	V_2
Switching Frequency	20kHz	f_s
Transformer Turn Ratio	1 : 1	n
HFL Equivalent Inductor	30uH	L
DC-link Capacitance	150uF	C_1, C_2
Load Resistance	10Ω ~ 100Ω	R

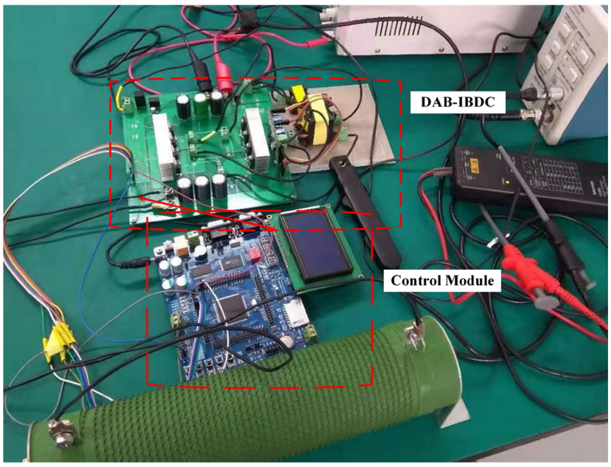

Figure 7: The prototype of DAB-IBDC.

(a)

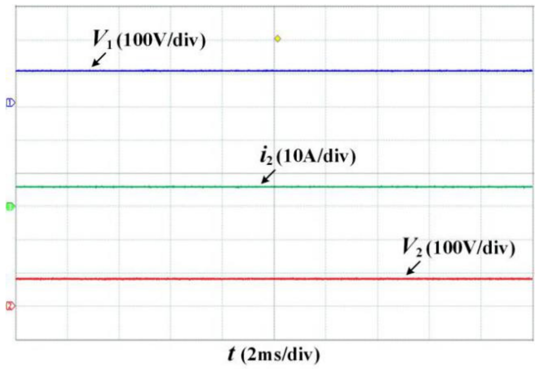

(b)

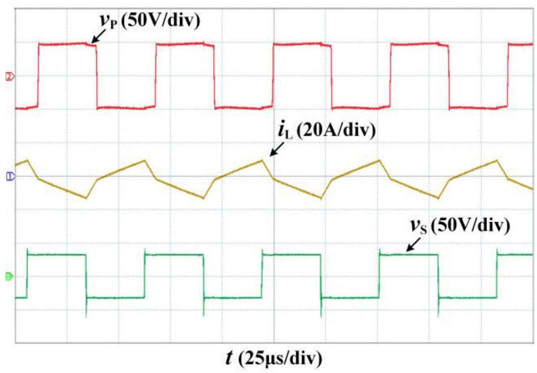

Figure 8: Experiment waveforms under SPS. (a) DC side voltages and current, (b) HFL voltages and current.

For the DAB-IBDC, Fig. 8 shows the steady-state experiment waveforms under SPS control. It can be seen that, the V_1 on the primary DC side is 100V, and the V_2 on the secondary DC side is regulated at the designed 80V. The HFL voltages v_P and v_S are both high-frequency square waves, and the frequencies of v_P, v_S and i_L are 20kHz. Besides, since the DC voltages deviate from the conversion ratio 1:1, the HFL current stress and reactive power become high. However, the SPS control could not solve this issue, and the maximum value of HFL current is 10.1A.

With the same transmission power, Fig. 9(a) and Fig. 9(b) show the experiment waveforms of DAB-IBDC under the conventional DPS control. It can be seen that the DAB-IBDC operates normally, i.e., V_1 is 100V and V_2 is also regulated at the designed 80V. Besides, the HFL current stress and reactive power under DPS control are lower than that under SPS control. Thus, the DPS strategy is able to improve the performance of the DAB-IBDC by reducing the maximum value of HFL current to 9.4A. Moreover, steady-state experiment waveforms of HFL current under conventional DPS and proposed optimized control are presented in Fig. 9(c) and Fig. 9(d). It can be seen that the conventional DPS with a larger inner phase-shift angle can further reduce the HFL current stress and reactive power, and the value of HFL current under the proposed optimized DPS control can reduce to 8.7A. Accordingly, the HFL current stress and reactive power under proposed optimized DPS control

(a)
(b)
(c)
(d)

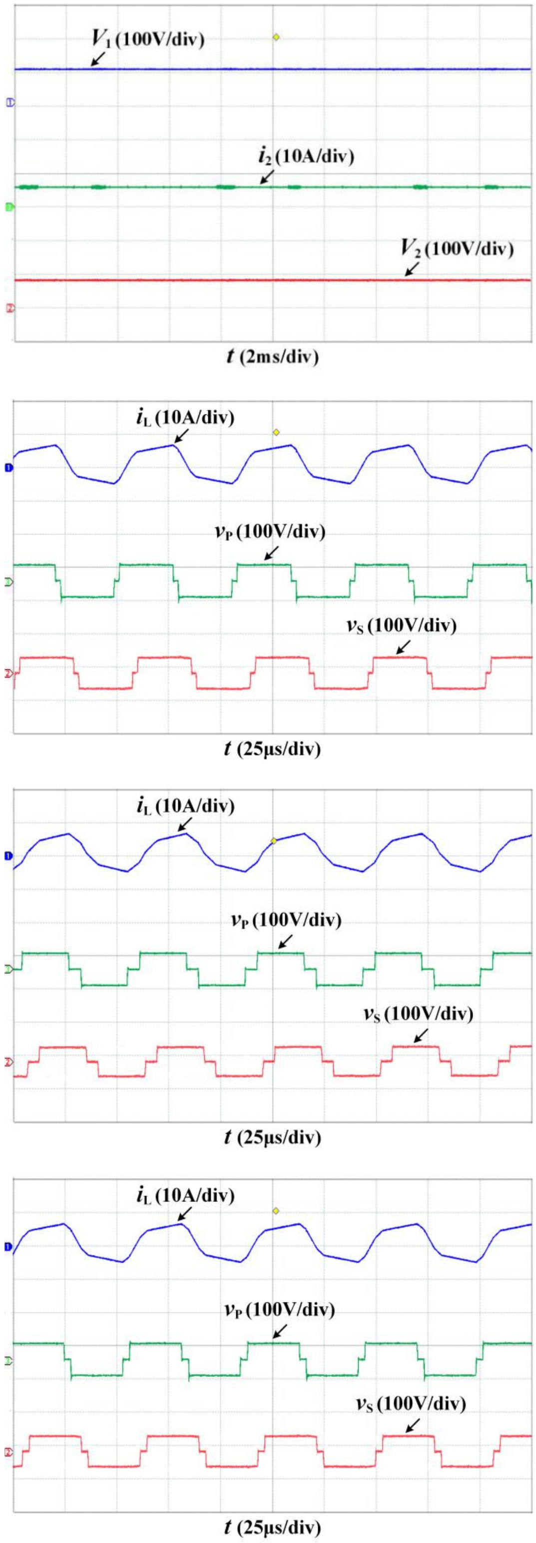

Figure 9: Experiment waveforms under conventional and proposed optimized DPS. (a) DC side Voltages and current of DAB-IBDC, (b) Conventional DPS when α = 0.12, (c) Conventional DPS when α = 0.25, (d) Proposed optimized DPS when α = 0.18.

(a)
(b)

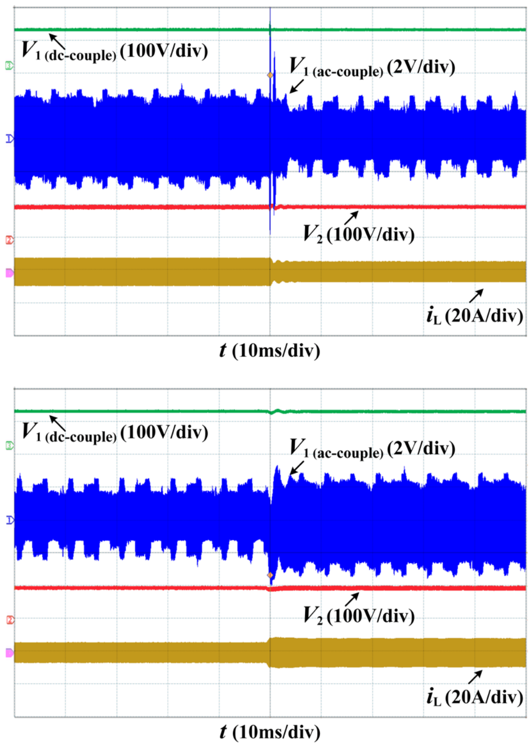

Figure 10: The dynamic-state experiment waveforms of DAB-IBDC under proposed optimized DPS strategy. (a) Load varies from 100% to 50%; (b) Load varies from 50% to 100%.

are lowest compared with that under SPS and conventional DPS.

The dynamic-state waveforms of the DAB-IBDC under the proposed optimized DPS strategy are presented in Fig. 10. According to Fig. 10(a), when the load varies from 100% to 50%, the voltage ripple of V_1 decreases, and V_2 maintains at 100V. Besides, the HFL current stress i_L decreases correspondingly. Similarly, when the load varies from 50% to 100%, the voltage ripple of V_1 increases, and V_2 keeps at 100V. In addition, the HFL current stress i_L increases correspondingly, according to Fig. 10(b). Based on the above analysis, it can be concluded that under the proposed optimized DPS strategy, the DC voltages on both sides of DAB-IBDC maintain at designed value, and the DAB-IBDC operates stably during the dynamic-state.

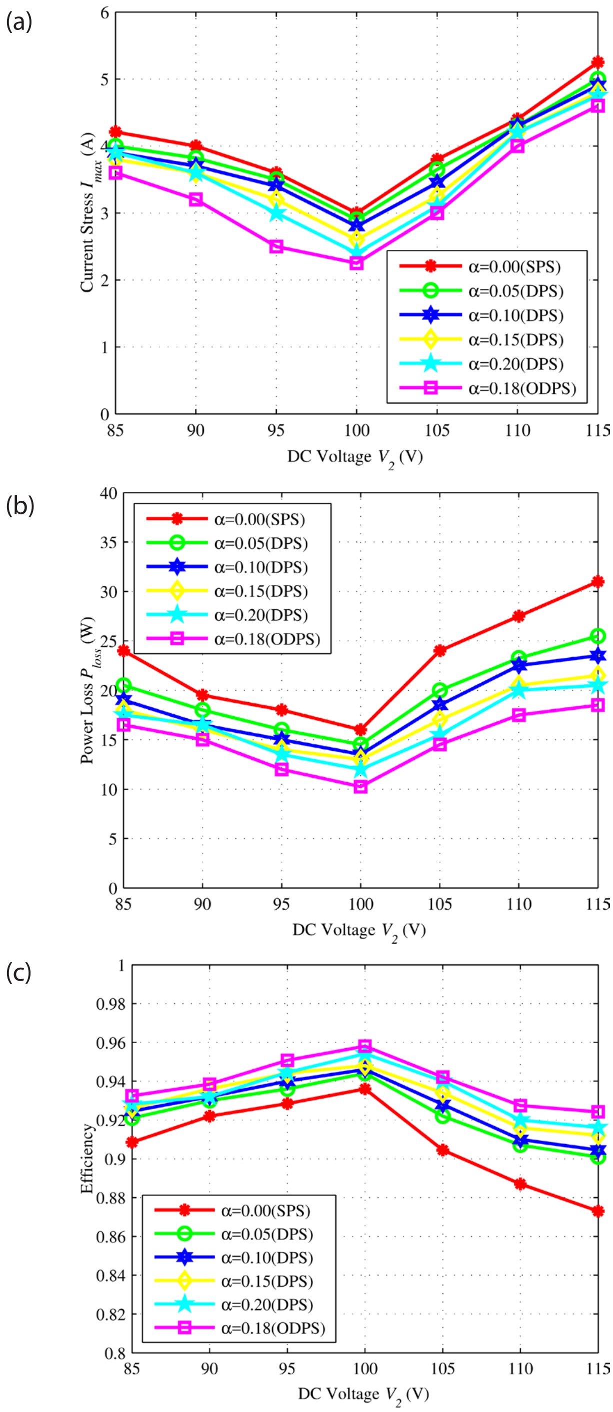

Figure 11: Experimental curves under conventional strategies and proposed optimized DPS (ODPS) strategy. (a) Curves of current stress, (b) Curves of power loss, (c) Curves of efficiency.

With the same transmission power and varied DC voltages, Fig. 11(a) shows the current stress of DAB-IBDC under conventional strategies and proposed optimized control strategy. From Fig. 11(a), it can be observed that: under the three control strategies, the lowest current stress occurs when *V*1 = *V*2 = 100V. However, the current stress would become higher because the conversion ratio deviates from 1:1 farther (e.g., *V*2 drops from 100V to 85V or increases from 100V to 115V). Also, the current stress under DPS control is lower than that under SPS control, and increasing the inner phase-shift angle can further reduce the current stress. In addition, the proposed optimized DPS strategy achieves the lowest current stress for DAB-IBDC among the three strategies.

Similarly, Fig. 11(b) and Fig. 11(c) present the power loss and efficiency of DAB-IBDC under conventional control strategies and proposed optimized control strategy, respectively. Similar to the results of current stress experiments, under various phase-shift control strategies, the lowest power loss can be achieved when *V*1 = *V*2 = 100V. Once *V*2 varies and deviates from the conversion ratio 1:1, it would result in larger power loss and lower efficiency. Meanwhile, lower power loss is achieved by the DPS strategy compared with that under the SPS strategy. Increasing the inner phase-shift angle α can further reduce power loss. In addition, the proposed optimized strategy realizes the lowest power loss, so as to obtain the highest efficiency for DAB-IBDC. Thus, the proposed multi-objective optimized strategy improves the efficiency of DAB-IBDC.

5 Conclusions

The DAB-IBDC plays a crucial role in DC distribution networks for realizing galvanic isolation, voltage conversion, power transfer, and bus connection. In this paper, the effect of phase-shift control on power transmission characteristic, current stress, and efficiency of DAB-IBDC is analyzed in detail. Then, to optimize these three features simultaneously, a DPS-based multi-objective optimized control strategy is proposed. The experiment results obtained from a built DAB-IBDC prototype verify that 1) the DPS control realizes less HFL reactive power, lower current stress, and higher efficiency for DAB-IBDC compared with SPS control, 2) the proposed optimized DPS control strategy optimizes the three features of DAB-IBDC simultaneously. Accordingly, the proposed control strategy can effectively improve the performance of DAB-IBDC, which makes it more adaptable and practical in DC power conversion networks.

6 Acknowledgments

This study was funded by the National Natural Science Foundation of China (No.51967012); Scientific Research and Innovation Team Project of Gansu Education Department (2018C-09); and State Grid Gansu Electric Power Company Project (SGGSKY00FJJS1800142).

7 Conflict of interest

The authors declare no conflict of interest. The founding sponsors had no role in the design of the study; in the collection, analyses, or interpretation of data; in the writing of the manuscript, and in the decision to publish the results.

8 References

1. T. Dragicevic, X. Lu, J. C. Vasquez, and J. M. Guerrero, "DC microgrids – part I: A review of control strategies and stabilization techniques," *IEEE Trans. Power Electron.*, vol. 31, no. 7, pp. 4876–4891, Jul. 2016. https://doi.org/10.1109/TPEL.2015.2478859
2. D. Liu, Y. Wang, F. Deng, and Z. Chen, "Balanced power device currents based modulation strategy for full-bridge three-level DC/DC converter," *IEEE Trans. Power Electron.*, vol. 35, no. 2, pp. 2008–2022, Feb. 2020. https://doi.org/10.1109/TPEL.2019.2918271
3. M. Mojibi and M. Radmehr, "Reliability evaluation of buck converter based on thermal analysis," *Inf. MIDEM*, vol. 48, no. 4, pp. 217–227, 2018. https://doi.org/10.33180/InfMIDEM2018.404
4. S. Ramasamy, I. R. Chandran, and C. Nallaperumal, "A High Voltage Gain Multiport Zeta-Zeta Converter for Renewable Energy Systems," *Inf. MIDEM*, vol. 50, no. 3, pp. 215–230, 2020. https://doi.org/10.33180/InfMIDEM2020.306
5. N. H. van der Blij, L. M. Ramirez-Elizondo, M. T. J. Spaan, and P. Bauer, "A state-space approach to modelling DC distribution systems," *IEEE Trans. Power Syst.*, vol. 33, no. 1, pp. 943–950, Jan. 2018. https://doi.org/10.1109/TPWRS.2017.2691547
6. Y. Wang, Q. Song, Q. Sun, B. Zhao, J. Li, and W. Liu, "Multilevel MVDC link strategy of high-frequency-link DC transformer based on switched capacitor for MVDC power distribution," *IEEE Trans. Ind. Electron.*, vol. 64, no. 4, pp. 2829–2835, Apr. 2017. https://doi.org/10.1109/TIE.2016.2643622
7. B. Zhao, Q. Song, W. Liu, and Y. Sun, "Overview of dual-active-bridge isolated bidirectional DC–DC converter for high-frequency-link power-conversion system," *IEEE Trans. Power Electron.*, vol. 29, no. 8, pp. 4091–4106, Aug. 2014. https://doi.org/10.1109/TPEL.2013.2289913
8. S. P. Engel, M. Stieneker, N. Soltau, S. Rabiee, H. Stagge, and R. W. D. Doncker, "Comparison of the modular multilevel DC converter and the dual-active bridge converter for power conversion in HVDC and MVDC grids," *IEEE Trans. Power Electron.*, vol. 30, no. 1, pp. 124–137, Jan. 2015. https://doi.org/10.1109/TPEL.2014.2310656
9. X. She, A. Q. Huang, and R. Burgos, "Review of solid-state transformer technologies and their application in power distribution systems," *IEEE J. Emerg. Sel. Top. Power Electron.*, vol. 1, no. 3, pp. 186–198, Sep. 2013. https://doi.org/10.1109/JESTPE.2013.2277917
10. Y. Wang, Q. Song, B. Zhao, J. Li, Q. Sun, and W. Liu, "Analysis and optimisation of modulation strategy based on dual-phase-shift for modular multilevel high-frequency-link DC transformer in medium-voltage DC distribution network," *IET Power Electron.*, vol. 11, no. 2, pp. 253–261, 2018. https://doi.org/10.1049/iet-pel.2016.0857
11. X. Xiang, X. Zhang, T. Luth, M. M. C. Merlin, and T. C. Green, "A compact modular multilevel DC–DC converter for high step-ratio MV and HV use," *IEEE Trans. Ind. Electron.*, vol. 65, no. 9, pp. 7060–7071, Sep. 2018. https://doi.org/10.1109/TIE.2018.2793249
12. K. Zhang, Z. Shan, and J. Jatskevich, "Large- and small-signal average-value modeling of dual-active-bridge DC–DC converter considering power losses," *IEEE Trans. Power Electron.*, vol. 32, no. 3, pp. 1964–1974, Mar. 2017. https://doi.org/10.1109/TPEL.2016.2555929
13. Y. Wang et al., "A multiple modular isolated DC/DC converter with bidirectional fault handling and efficient energy conversion for DC distribution network," *IEEE Trans. Power Electron.*, vol. 35, no. 11, pp. 11502–11517, Nov. 2020. https://doi.org/10.1109/TPEL.2020.2985232
14. S. Chowdhury, P. W. Wheeler, C. Gerada, and C. Patel, "Model predictive control for a dual-active bridge inverter with a floating bridge," *IEEE Trans.*

Ind. Electron., vol. 63, no. 9, pp. 5558–5568, Sep. 2016.
https://doi.org/10.1109/TIE.2016.2564949
15. J. Riedel, D. G. Holmes, B. P. McGrath, and C. Teixeira, "ZVS soft switching boundaries for dual active bridge DC–DC converters using frequency domain analysis," *IEEE Trans. Power Electron.*, vol. 32, no. 4, pp. 3166–3179, Apr. 2017.
https://doi.org/10.1109/TPEL.2016.2573856
16. J. D. Páez, D. Frey, J. Maneiro, S. Bacha, and P. Dworakowski, "Overview of DC–DC converters dedicated to HVDC grids," *IEEE Trans. Power Deliv.*, vol. 34, no. 1, pp. 119–128, Feb. 2019.
https://doi.org/10.1109/TPWRD.2018.2846408
17. X. Li and Y. Li, "An optimized phase-shift modulation for fast transient response in a dual-active-bridge converter," *IEEE Trans. Power Electron.*, vol. 29, no. 6, pp. 2661–2665, Jun. 2014.
https://doi.org/10.1109/TPEL.2013.2294714
18. B. Zhao, Q. Song, W. Liu, and Y. Zhao, "Transient DC bias and current impact effects of high-frequency-isolated bidirectional DC–DC converter in practice," *IEEE Trans. Power Electron.*, vol. 31, no. 4, pp. 3203–3216, Apr. 2016.
https://doi.org/10.1109/TPEL.2015.2445831
19. N. Hou, W. Song, and M. Wu, "Minimum-current-stress scheme of dual active bridge DC–DC converter with unified phase-shift control," *IEEE Trans. Power Electron.*, vol. 31, no. 12, pp. 8552–8561, Dec. 2016.
https://doi.org/10.1109/TPEL.2016.2521410
20. B. Zhao, Q. Song, W. Liu, and W. Sun, "Current-stress-optimized switching strategy of isolated bidirectional DC–DC converter with dual-phase-shift control," *IEEE Trans. Ind. Electron.*, vol. 60, no. 10, pp. 4458–4467, Oct. 2013.
https://doi.org/10.1109/TIE.2012.2210374
21. G. Oggier, G. O. García, and A. R. Oliva, "Modulation strategy to operate the dual active bridge DC-DC converter under soft switching in the whole operating range," *IEEE Trans. Power Electron.*, vol. 26, no. 4, pp. 1228–1236, Apr. 2011.
https://doi.org/10.1109/TPEL.2010.2072966
22. A. Rodríguez, A. Vázquez, D. G. Lamar, M. M. Hernando, and J. Sebastián, "Different purpose design strategies and techniques to improve the performance of a dual active bridge with phase-shift control," *IEEE Trans. Power Electron.*, vol. 30, no. 2, pp. 790–804, Feb. 2015.
https://doi.org/10.1109/TPEL.2014.2309853
23. F. Krismer and J. W. Kolar, "Efficiency-optimized high-current dual active bridge converter for automotive applications," *IEEE Trans. Ind. Electron.*, vol. 59, no. 7, pp. 2745–2760, Jul. 2012.
https://doi.org/10.1109/TIE.2011.2112312
24. B. Zhao, Q. Song, and W. Liu, "Efficiency characterization and optimization of isolated bidirectional DC–DC converter based on dual-phase-shift control for DC distribution application," *IEEE Trans. Power Electron.*, vol. 28, no. 4, pp. 1711–1727, Apr. 2013.
https://doi.org/10.1109/TPEL.2012.2210563
25. H. Bai, Z. Nie, and C. C. Mi, "Experimental comparison of traditional phase-shift, dual-phase-shift, and model-based control of isolated bidirectional DC–DC converters," *IEEE Trans. Power Electron.*, vol. 25, no. 6, pp. 1444–1449, Jun. 2010.
https://doi.org/10.1109/TPEL.2009.2039648
26. A. K. Jain and R. Ayyanar, "PWM control of dual active bridge: Comprehensive analysis and experimental verification," *IEEE Trans. Power Electron.*, vol. 26, no. 4, pp. 1215–1227, Apr. 2011.
https://doi.org/10.1109/TPEL.2010.2070519
27. S. S. Muthuraj, V. K. Kanakesh, P. Das, and S. K. Panda, "Triple phase shift control of an LLL tank based bidirectional dual active bridge converter," *IEEE Trans. Power Electron.*, vol. 32, no. 10, pp. 8035–8053, Oct. 2017.
https://doi.org/10.1109/TPEL.2016.2637506
28. A. Taylor, G. Liu, H. Bai, A. Brown, P. M. Johnson, and M. McAmmond, "Multiple-phase-shift control for a dual active bridge to secure zero-voltage switching and enhance light-load performance," *IEEE Trans. Power Electron.*, vol. 33, no. 6, pp. 4584–4588, Jun. 2018.
https://doi.org/10.1109/TPEL.2017.2769638
29. Y. Wang, Q. Song, B. Zhao, J. Li, Q. Sun, and W. Liu, "Quasi-square-wave modulation of modular multilevel high-frequency DC converter for medium-voltage DC distribution application," *IEEE Trans. Power Electron.*, vol. 33, no. 9, pp. 7480–7495, Sep. 2018.
https://doi.org/10.1109/TPEL.2017.2772833
30. I. A. Gowaid, G. P. Adam, S. Ahmed, D. Holliday, and B. W. Williams, "Analysis and design of a modular multilevel converter with trapezoidal modulation for medium and high voltage DC-DC transformers," *IEEE Trans. Power Electron.*, vol. 30, no. 10, pp. 5439–5457, Oct. 2015.
https://doi.org/10.1109/TPEL.2014.2377719
31. Y. Yan, H. Bai, A. Foote, and W. Wang, "Securing full-power-range zero-voltage switching in both steady-state and transient operations for a dual-active-bridge-based bidirectional electric vehicle charger," *IEEE Trans. Power Electron.*, vol. 35, no. 7, pp. 7506–7519, Jul. 2020.
https://doi.org/10.1109/TPEL.2019.2955896
32. Q. Gu, L. Yuan, J. Nie, J. Sun and Z. Zhao, "Current stress minimization of dual-active-bridge DC-DC converter within the whole operating range," *IEEE*

J. Emerg. Sel. Top. Power Electron., vol. 7, no. 1, pp. 129–142, Mar. 2019.
https://doi.org/10.1109/JESTPE.2018.2886459

33. O. M. Hebala, A. A. Aboushady, K. H. Ahmed and I. Abdelsalam, "Generic closed-loop controller for power regulation in dual active bridge DC-DC converter with current stress minimization," *IEEE Trans. Ind. Electron.*, vol. 66, no. 6, pp. 4468–4478, Jun. 2019.
https://doi.org/10.1109/TIE.2018.2860535

Arrived: 31. 01. 2021
Accepted: 23. 08. 2021

第 18 卷 第 1 期　　　　电　源　学　报　　　　Vol.18 No.1
2020 年 1 月　　　　Journal of Power Supply　　　　Jan. 2020

DOI:10.13234/j.issn.2095-2805.2020.1.116　　　　中图分类号:TM46　　　　文献标志码:A

应用于模块化多电平直流变换器的阶梯波调制策略

徐晓冬 [1],包广清 [1],马　明 [2,3],汪宁渤 [2,3],王　裕 [4]

(1. 兰州理工大学电气工程与信息工程学院,兰州 730050;2. 国网甘肃省电力公司电力科学研究院,兰州 730070;3. 甘肃省新能源并网运行控制重点实验室,兰州 730070;4. 广东工业大学自动化学院,广州 510006)

摘要:在直流配电网中,模块化多电平直流变换器 MDCC(modular multilevel DC/DC converter)以模块化多电平变换器结构为基础,是实现不同电压等级直流母线电压变换和电能双向传输的核心装置。探讨 MDCC 的高频链阶梯波调制策略,并采用傅里叶级数建模,可有效简化阶梯波建模和分析过程。此外,阶梯波调制可有效减小高频链电压 dv/dt、谐波和无功含量,提升 MDCC 整体效率,促进 MDCC 在直流配电网中的应用。

关键词:直流配电网;模块化多电平直流变换器;阶梯波调制

Staircase Triangular Modulation Strategy for Modular Multilevel DC/DC Converter

XU Xiaodong[1], BAO Guangqing[1], MA Ming[2,3], WANG Ningbo[2,3], WANG Yu[4]

(1. College of Electrical and Information Engineering, Lanzhou University of Technology, Lanzhou 730050, China; 2. Electric Power Research Institute, State Grid Gansu Electric Power Company, Lanzhou 730070, China; 3. Gansu Key Laboratory of Wind Power Integration Operation and Control, Lanzhou 730070, China; 4. School of Automation, Guangdong University of Technology, Guangzhou 510006, China)

Abstract: In a DC distribution network, based on the structure of a modular multilevel converter (MMC), the modular multilevel DC/DC converter (MDCC) is a key device for realizing the voltage conversion and bidirectional power transmission between DC buses of different voltage levels. The staircase triangular modulation (STM) strategy for high-frequency link (HFL) in MDCC is analyzed. With Fourier series, the modeling and analysis process of STM can be effectively simplified. In addition, STM can effectively reduce the dv/dt and content of harmonics and reactive power in HFL voltages, improving the overall efficiency of MDCC and promoting its applications in DC distribution network.

Keywords: DC distribution network; modular multilevel DC/DC converter; staircase triangular modulation

随着分布式电源的发展,直流配电网可以发挥直流配电的技术优势, 有效减少不必要的转换环节,方便新能源、储能系统和直流负荷的接入,降低配电系统的复杂程度和成本,改善电能质量,提高电能转换和传输效率,因而已成为学术界和电力行业的重要研究课题[1-3]。其中,直流变压器 DCT(DC transformer) 是实现直流配电网不同电压等级直流母线电压变换和电能双向传输的核心装置[4-5]。

在低压小功率领域,DCT 最普遍采用的是双有源全桥 DAB(dual active bridge)拓扑结构[6-8]。为了提升DCT 的电压等级和功率容量,有效进行电压变

收稿日期:2019-10-17;修回日期:2019-12-31
基金项目:国家自然科学基金资助项目(51967012);甘肃省教育厅科学研究创新团队资助项目(2018C-09);国家电网科技资助项目(SGGSKY00FJJS1800142)
Project Supported by National Natural Science Foundation of China(51967012); Scientific Research and Innovation Team Project of Gansu Education Department(2018C-09); State Grid Gansu Electric Power Company Project(SGGSKY00FJJS1800142)

换及电能传输，在模块化多电平变换器 MMC(modular multilevel converter)拓扑结构的基础上提出的模块化多电平直流变换器 MDCC(modular multilevel DC/DC converter)备受关注[9-10]。为更好地连接中高压与低压直流母线，文献[11]提出了一种基于 MMC 和全桥变换器结构的 MDCC 拓扑，目前，对于 MDCC 的研究主要集中于拓扑结构、控制方法、高频链 HFL(high-frequency link)调制和联网运行等。其中，方波调制是 HFL 调制常用的调制方式，可有效提升直流电压利用率和功率传输能力，但也因此造成较大 dv/dt，而且方波电压存在大量谐波和无功成分，降低变换器效率，不利于推广应用[12]；此外，阶梯波调制可有效减轻变压器上的 dv/dt 应力，并降低 HFL 电压中的谐波含量，对基于 MMC 的模块化多电平直流变换器的 HFL 调制有了初步的探讨[13-14]。然而，对于 MDCC 这种不对称拓扑的直流变换器的阶梯波调制仍未见报道。

本文将阶梯波调制方式应用到 MDCC 的 HFL 调制中，并采用傅里叶级数建模，可有效简化阶梯波调制方式的建模和分析过程。此外，采用阶梯波调制方式，可有效减小 HFL 电压的 dv/dt、谐波和无功含量，提升 MDCC 整体效率，更好地在直流配电网中实现电压变换和电能传输。

1 MDCC 的 HFL 阶梯波调制

1.1 MDCC 拓扑结构

本文所采用的 MDCC 拓扑结构如图 1 所示。MDCC 中高压侧采用单相 MMC 结构，每个桥臂由 n 个半桥子模块 SM(sub-module)和 1 个电感 L_s 串联而成，可有效提高电压和功率等级；低压侧采用 m 个全桥变换器并联，以提升电流等级；高频链由多个高频隔离变压器串联而成。MDCC 半桥 SM 和全桥变换器的数量都可以根据实际应用中电压和功率等级进行调整。V_{MV} 和 I_{MV} 分别为中高压侧电

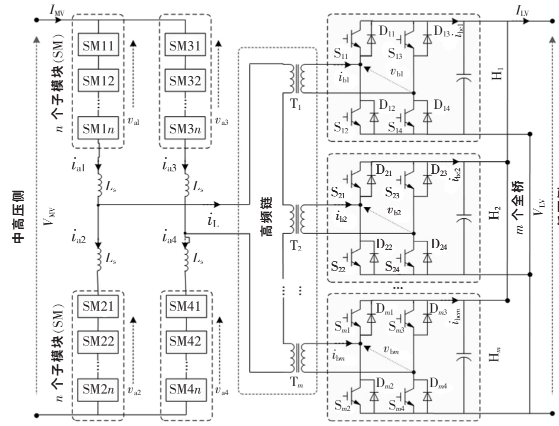

图 1 MDCC 拓扑结构

Fig.1 Topology of MDCC

压和电流，V_{LV} 和 I_{LV} 分别为低压侧电压和电流；v_{aij} 和 V_{ij} 分别为半桥子模块在交流侧和直流侧的电压，v_{a1}~v_{a4} 和 i_{a1}~i_{a4} 分别为 MMC 桥臂电压和电流；i_L 为高频链电流；v_{bi} 和 i_{bi} 分别为全桥模块交流侧电压和电流，i_{bci} 为全桥模块直流侧电流。

为了产生理想的 HFL 阶梯波，在中高压侧 MMC 结构的同一桥臂相邻的 SM 之间加入 π/n 的移相角，在低压侧相邻全桥变换器之间加入 π/m 的移相角。子模块电压叠加形成桥臂电压，从而形成高频链电压 v_a；全桥模块电压 v_{bi} 形成高频链电压 v_b；2 个高频链电压的差加在高频电感上产生高频链电流 i_L。为保证子模块间直流侧电压的平衡，本文采用文献[15]所提子模块电压交替平衡算法，有效降低了电压平衡算法的复杂度。

1.2 MDCC 阶梯波调制建模与特性分析

MDCC 结构和控制复杂，使时域分析中产生的波形分段过多，为避免因此导致的分段函数复杂且难以分析和计算的问题，采用傅里叶级数变换方法，使得 HFL 调制的分析从时域转到频域，进行 HFL 电气量分析和数学建模。

采用傅里叶级数进行描述，HFL 电压 v_a 和 v_b 可分别表示为

$$\begin{cases} v_a(t)=\sum\limits_{k=1,3,5,\cdots}\dfrac{4V_{MV}}{kn\pi}\cos\left(\dfrac{k\alpha_1}{2}\right)\sum\limits_{i=0}^{n-1}\sin\left[k\left(\omega t+i\dfrac{\pi}{n}\right)\right]=\sum\limits_{k=1,3,5,\cdots}\dfrac{4V_{MV}}{k\pi n}\cos\left(\dfrac{k\alpha_1}{2}\right)\dfrac{\sin\left(\dfrac{k\pi}{2}\right)\sin k\left[\omega t+\dfrac{(n-1)\pi}{2n}\right]}{\sin\left(\dfrac{k\pi}{2n}\right)} \\ v_b(t)=\sum\limits_{k=1,3,5,\cdots}\dfrac{4n_TV_{LV}}{k\pi}\cos\left(\dfrac{k\alpha_2}{2}\right)\sum\limits_{i=0}^{n-1}\sin\left[k\left(\omega t-\beta+i\dfrac{\pi}{m}\right)\right]=\sum\limits_{k=1,3,5,\cdots}\dfrac{4n_TV_{LV}}{k\pi}\cos\left(\dfrac{k\alpha_2}{2}\right)\dfrac{\sin\left(\dfrac{k\pi}{2}\right)\sin k\left[\omega t-\beta+\dfrac{(m-1)\pi}{2m}\right]}{\sin\left(\dfrac{k\pi}{2m}\right)} \end{cases} \quad (1)$$

式中：n_T 为高频链变压器电压变比；n 为子模块数；α_1 和 α_2 为内相移角；β 为初级和次级 HFL 电压之间的相移角。当 $\alpha_1=\alpha_2=0$ 时为单移相控制SPS（single-phase shift）；当 $\alpha_1=0$、$\alpha_2\neq0$ 或 $\alpha_2=0$、$\alpha_1\neq0$ 时为扩展移相控制 EPS（extend-phase shift）；当 $\alpha_1=\alpha_2=\alpha$ 时为双移相控制 DPS（dual-phase shift）。

应用于 MDCC 的阶梯波调制波形见图 2，开关频率 f_s=20 kHz。由图可知，HFL 电压阶跃被限制为 1 个 SM 或全桥变换器模块电压，有效地降低了 dv/dt。

此外，MDCC 可等效为 2 个交流电压源连接在电感两端，且根据 HFL 电流在 1 个开关周期的对称性，HFL 电流可表示为

$$i_L(t)-i_L(0)=\int_0^t \frac{v_a(t)-v_b(t)}{L}\mathrm{d}t \tag{2}$$

结合稳态条件时电感电流开关周期平均值为 0，由式（1）可得 HFL 电流为

$$\begin{cases} i_L(t)=\displaystyle\sum_{k=1,3,5,\cdots}\frac{2\sin\left(\frac{k\pi}{2}\right)}{k^2\pi\omega L}\sqrt{A^2+B^2}\sin\left(k\omega t+\arctan\frac{A}{B}\right) \\ A=\cos\left(\frac{k\alpha_2}{2}\right)n_T V_{LV}m\cos k\left[-\beta+\frac{(m-1)\pi}{2m}\right]- \\ \quad \cos\left(\frac{k\alpha_1}{2}\right)V_{MV}\cos k\frac{(n-1)\pi}{2n} \\ B=-\cos\left(\frac{k\alpha_2}{2}\right)n_T V_{LV}m\sin k\left[-\beta+\frac{(m-1)\pi}{2m}\right]+ \\ \quad \cos\left(\frac{k\alpha_1}{2}\right)V_{MV}\sin k\frac{(n-1)\pi}{2n} \end{cases} \tag{3}$$

在平衡的三相系统中，由于对称关系，偶次谐波被消除得非常小，所以主要存在的是奇次谐波。因此，除了基波分量外，HFL 电压和电流主要含有奇次谐波分量，HFL 电压电流和有效值可以分别描述为

$$\begin{cases} V_{arms}=\sqrt{\displaystyle\sum_{k=1,3,5,\cdots}V_{ak}^2}=\sqrt{\displaystyle\sum_{k=1,3,5,\cdots}\left[\frac{2\sqrt{2}\,V_{MV}}{kn\pi\sin\left(\frac{k\pi}{2n}\right)}\right]^2} \\ V_{brms}=\sqrt{\displaystyle\sum_{k=1,3,5,\cdots}V_{bk}^2}=\sqrt{\displaystyle\sum_{k=1,3,5,\cdots}\left[\frac{2\sqrt{2}\,n_T V_{LV}}{k\pi\sin\left(\frac{k\pi}{2m}\right)}\right]^2} \\ I_{arms}=\sqrt{\displaystyle\sum_{k=1,3,5,\cdots}I_k^2}=\sqrt{\displaystyle\sum_{k=1,3,5,\cdots}\left(\frac{2\sqrt{2}}{k^2\pi w_0 L}\sqrt{A^2+B^2}\right)^2} \end{cases} \tag{4}$$

由式（1）~式（4）可得，1 个开关周期内 MDCC 的平均传输功率为

$$P=\frac{1}{T}\int_0^T v_a(t)i_L(t)\mathrm{d}t \tag{5}$$

由此，有功功率仅仅是由相同频率的电压和电流分量产生，可以表示为

$$P=\sum_{k=1,3,5,\cdots}\frac{4V_{MV}V_{LV}n_T m\sin^2\left(\frac{k\pi}{2}\right)}{k^3\pi^2\omega L}\cos\left(\frac{k\alpha_1}{2}\right)\cdot \cos\left(\frac{k\alpha_2}{2}\right)\sin(k\beta) \tag{6}$$

无功功率可以通过相同频率和不同频率的电压和电流分量来产生，即

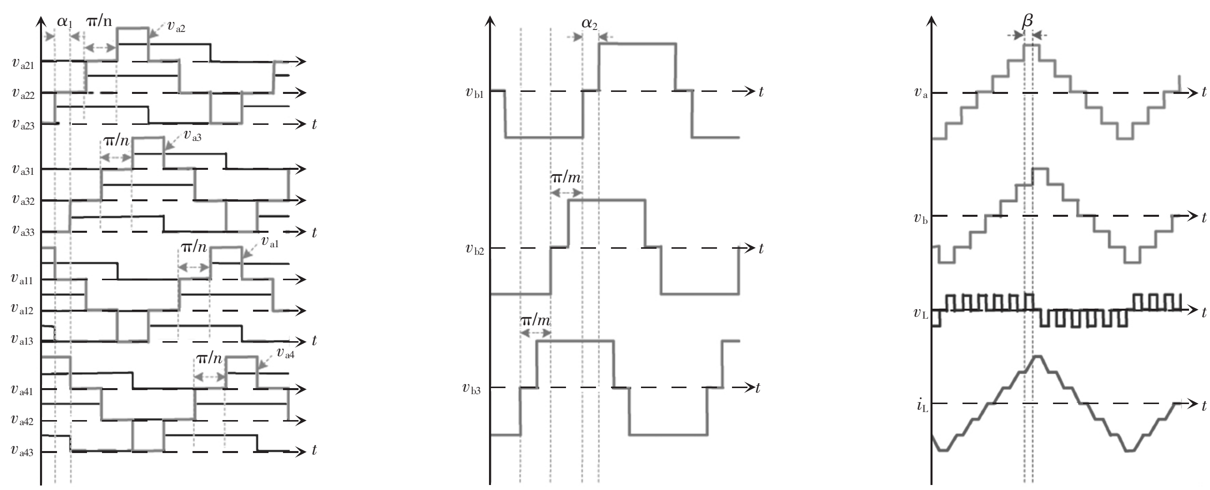

（a）中高压侧 MMC 子模块调制波形　　（b）低压侧全桥模块调制波形　　（c）高频链电压和电流波形

图 2　HFL 阶梯波调制波形

Fig.2 Waveforms of HFL under staircase triangular modulation

$$
\begin{cases}
Q_{k_1\neq k_2=k}=\sum\limits_{k=1,3,5,\cdots}\dfrac{4V_{\mathrm{MV}}V_{\mathrm{LV}}n_{\mathrm{T}}m\sin^2\left(\dfrac{k\pi}{2}\right)}{k^3\pi^2\omega L}\cos\left(\dfrac{k\alpha_1}{2}\right)\cdot \\
\qquad\left[M\cos\left(\dfrac{k\alpha_1}{2}\right)-\cos\left(\dfrac{k\alpha_2}{2}\right)\cos(k\beta)\right] \\
Q_{k_1\neq k_2}=U_{ak_1}I_{Lk_2}=\dfrac{4V_{\mathrm{MV}}\sin^2\left(\dfrac{k_1\pi}{2}\right)}{k_1k_2^2\pi^2\omega L}\cos\left(\dfrac{k_1\alpha_1}{2}\right)\cdot \\
\qquad\sqrt{A^2+B^2}
\end{cases} \tag{7}
$$

式中：M 为 MDCC 的电压变换比，$M=V_{\mathrm{MV}}/mn_{\mathrm{T}}V_{\mathrm{LV}}$。

由式(5)~式(7)可得 MDCC 的视在功率 S 为

$$S=\sqrt{\sum_{k=1,3,5,\cdots}P_k^2+\sum_{k=1,3,5,\cdots}Q_k^2+\sum_{k=1,3,5,\cdots}Q_{k_1\neq k_2}^2} \tag{8}$$

因此，由式(5)~式(8)可得 MDCC 的 HFL 功率因数为

$$\lambda=\frac{P}{S} \tag{9}$$

由式(1)可看出，采用阶梯波调制，HFL 电压波形接近正弦波，电压的谐波含量降低；进而由式(3)~式(7)可得无功功率含量也相应降低。此外，根据式(7)~式(9)，外移相角 β 及内移相角 α($\alpha_1=\alpha_2=\alpha$)对 HFL 功率因数的影响如图 3 所示，选取 $\alpha=0$ 对应 SPS 控制，$\alpha=0.2$ 对应 DPS 控制。可以看出，通过调节外移相角和内移相角，能有效调节 MDCC 的传输功率、无功功率和功率因数，从而进一步抑制 HFL 谐波和无功功率，降低损耗，提升 MDCC 整体效率。

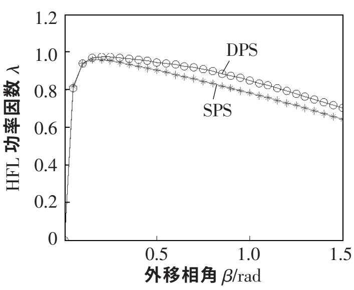

图 3　MDCC 的 HFL 功率特性

Fig.3 HFL power characteristics of MDCC

2　实验验证

为了有效验证理论分析，在实验室环境搭建了 1 台 MDCC 样机，如图 4 所示，其参数如表 1 所示。

采用阶梯波调制时，稳态下 MDCC 的实验波形如图 5 所示。可见，MDCC 中高压侧电压稳定在 300 V；低压侧电压稳定在 130 V；HFL 电压 v_{a} 和 v_{b} 均为阶梯波，v_{a}、v_{b} 和电流 i_{L} 的频率均为 20 kHz。对比方波调制，阶梯波调制的 HFL 电压接近正弦波，且随着 SM 和全桥变换器数量的增加，高频链电压愈发呈现正弦波状；其 HFL 电压的谐波含量也大为降低。

采用阶梯波调制时，MDCC 两端的 SM 和全桥变换器电压波形如图 6 所示。从图中可以看出，各 SM 方波电压 v_{a11}，v_{a12}，v_{a13} 的幅值相等，均为 V_{dc}；且相邻 SM 电压的相角差为 π/3，使得 HFL 电压 v_{a} 呈阶梯波升降。区别于传统方波调制，阶梯波调制使每个 SM 电压幅值下降为 V_{MV}/n=300/3=100 V，加在 HFL 变压器的 dv/dt 也从方波调制的300 V 下降为阶梯波调制的 100 V，有效降低了高频电压的 dv/dt 以及开关管的压降。其次，低压侧的全桥变换器产生相同幅值的方波电压 v_{b1}、v_{b2} 和v_{b3}，并直接构成 HFL 电压 v_{b}。最后，构成 MDCC 的SM 和全桥变换器

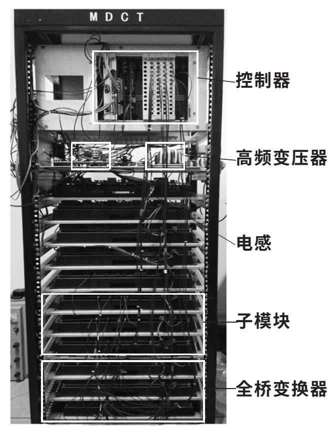

图 4　MDCC 实验样机

Fig.4 Experimental prototype of MDCC

表 1　实验样机参数

Tab.1 Parameters of experimental prototype

参数	数值	参数	数值
高压侧电压/V	300	变压器漏感/μH	42
低压侧电压/V	115~145	桥臂电感/μH	31
开关频率/kHz	20	变压器变比	4:5
桥臂子模块数	3	子模块电容/μF	470

均处于均压状态，确保了 MDCC 的正常运行。

阶梯波调制下，当低压侧电压变化时，选择不同内移相角 α 的 MDCC 整体效率如图 7 所示。由图可知，当低压侧电压为 130 V 时，MDCC 两端电压比与 HFL 变压器变比吻合，变换器整体效率最高；而随着低压侧电压偏离 130 V，MDCC 整体效率降低。此外，当 $\alpha\neq0$(DPS 控制)时，MDCC 的整体效率都比 α=0(SPS 控制)时高，并与 α 成正比。因此，采用包含内移相角的阶梯波调制方式，可有效降低高频链电压 dv/dt、谐波和无功含量，提升 MDCC 的整体效率。

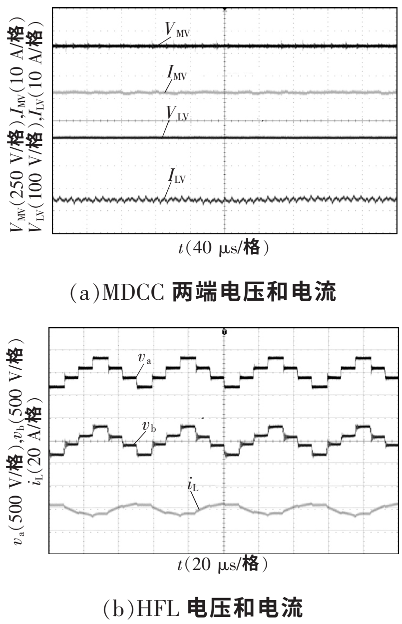

图 5 阶梯波调制下 MDCC 稳态运行实验波形

Fig.5 Experimental waveforms of MDCC steady-state operation under staircase triangular modulation

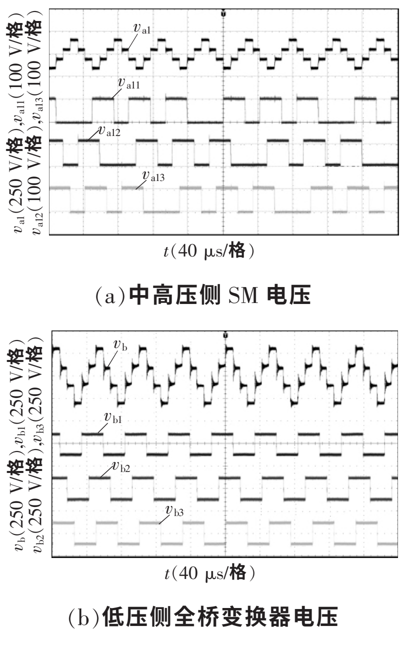

图 6 阶梯波调制下 MDCC 两端 SM 和全桥变换器电压

Fig.6 Voltages of SMs at two terminals of MDCC and full-bridge converter under staircase triangular modulation

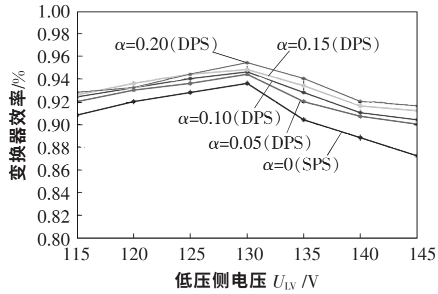

图 7 阶梯波调制下移相角与 MDCC 整体效率

Fig.7 Overall efficiency of MDCC with phase-shift angle under staircase triangular modulation

3 结语

本文分析了 MDCC 的 HFL 阶梯波调制方式。采用傅里叶级数建模，可有效简化阶梯波调制的建模和分析过程。相较于常用的方波调制方式，阶梯波调制可有效减小 HFL 电压的 dv/dt，降低其谐波和无功含量，提升 MDCC 的整体效率，更好地在直流配电网中实现电压变换和电能传输。

参考文献：

[1] Tabari M, Yazdan A. Stability of a dc distribution system for power system integration of plug-in hybrid electric vehicles[J]. IEEE Transactions on Smart Grid, 2014, 5(5): 2564-2573.

[2] 宋强, 赵彪, 刘文华, 等. 智能直流配电网研究综述[J]. 中国电机工程学报, 2013, 33(25): 9-19.
Song Qiang, Zhao Biao, Liu Wenhua, et al. An overview of research on smart DC distribution power network[J]. Proceedings of the CSEE, 2013, 33(25): 9-19(in Chinese).

[3] 江道灼, 郑欢. 直流配电网研究现状与展望[J]. 电力系统自动化, 2012, 36(8): 98-106.
Jiang Daozhuo, Zheng Huan. Research status and develop-

ing prospect of DC distribution network[J]. Automation of Electric Power Systems, 2012, 36(8): 98-106(in Chinese).

[4] Engel S P, Stieneker M, Soltau N, et al. Comparison of the modular multilevel DC converter and the dual-active bridge converter for power conversion in HVDC and MVDC grids[J]. IEEE Transactions on Power Electronics, 2015, 30(1): 124-137.

[5] Zhao Biao, Song Qiang, Liu Wenhua, et al. Overview of dual-active-bridge isolated bidirectional dc-dc converter for high-frequency-link power-conversion system[J]. IEEE Transactions on Power Electronics, 2014, 29(8): 4091-4106.

[6] Krismer F, Kolar J. Efficiency-optimized high-current dual active bridge converter for automotive applications[J]. IEEE Transactions on Power Electronics, 2012, 59(7): 2745-2760.

[7] 孙谦浩, 王裕, 宋强. 应用于直流配电网的双向全桥 DC/DC 变换器比较分析[J]. 电力自动化设备, 2017, 37(10): 49-56.
Sun Qianhao, Wang Yu, Song Qiang, et al. Analysis and comparison of dual-active-bridge DC/DC converters in DC distribution network[J]. Electric Power Automation Equipment, 2017, 37(10): 49-56(in Chinese).

[8] 张勋, 王广柱, 商秀娟, 等. 双向全桥 DC-DC 变换器回流功率优化的双重移相控制[J]. 中国电机工程学报, 2016, 36(4): 1090-1097.
Zhang Xun, Wang Guangzhu, Shang Xiujuan, et al. An optimized strategy based on backflow power of bi-directional dual-active-bridge DC-DC converters with dual-phase-shifting control[J]. Proceedings of the CSEE, 2016, 36(4): 1090-1097(in Chinese).

[9] Kenzelmann S, Rufer A, Dujic D, et al. Isolated DC/DC structure based on modular multilevel converter[J]. IEEE Transactions on Power Electronics, 2015, 30(1): 89-98.

[10] Kish G J, Ranjram M, Lehn P W. A modular multilevel DC/DC converter with fault blocking capability for HVDC interconnects[J]. IEEE Transactions on Power Electronics, 2015, 30(1): 148-162.

[11] Zhao Biao, Song Qiang, Li Jianguo, et al. Modular multilevel high-frequency-link DC transformer based on dual active phase-shift principle for medium-voltage DC power distribution application[J]. IEEE Transactions on Power Electronics, 2017, 32(3): 1779-1791.

[12] Zhao Biao, Song Qiang, Li Jianguo, et al. High-frequency-link modulation methodology of DC-DC transformer based on modular multilevel converter for HVDC application: Comprehensive analysis and experimental verification[J]. IEEE Transactions on Power Electronics, 2017, 32(5): 3413-3424.

[13] Gowaid I A, Adam G P, Ahmed S, et al. Analysis and design of a modular multilevel converter with trapezoidal modulation for medium and high voltage DC-DC transformers[J]. IEEE Transactions on Power Electronics, 2015, 30(10): 5439-5457.

[14] Wang Yu, Song Qiang, Zhao Biao, et al. Quasi-square-wave modulation of modular multilevel high-frequency DC converter for medium-voltage DC distribution application[J]. IEEE Transactions on Power Electronics, 2018, 33(9): 7480-7495.

[15] Sun Qianhao, Wei Yingdong, Wang Yu, et al. Optimized control strategy of modular multilevel DC transformer for high-frequency-link voltages matching in the whole operation range[J]. IEEE Journal of Emerging and Selected Topics in Power Electronics, 2019, Accepted.

徐晓冬

作者简介：

徐晓冬（1983–），男，博士研究生，讲师，研究方向：双向 DC/DC 变换器设计与控制，E-mail：xu-xiao-dong@foxmail.com。

包广清（1972–），女，通信作者，博士，教授，研究方向：特种电机设计和新能源并网稳定性，E-mail：gqbao@lut.cn。

马明（1983–），男，硕士，工程师，研究方向：电力系统运行及新能源发电，E-mail：ming-ma@foxmail.com。

汪宁渤（1963–），男，硕士，教授级高级工程师，研究方向：新能源发电与并网运行控制技术，E-mail：wangnb@gs.sgcc.com.cn。

王裕（1984–），男，中国电源学会高级会员，博士，副教授，研究方向：直流配电网和直流变压器，E-mail：yuwang@gdut.edu.cn。